Effective masses, lifetimes, and optical conductivity in Sr_2RuO_4 and $Sr_3Ru_2O_7$: Interplay of spin-orbit, crystal-field, and Coulomb tetragonal tensor interactions

Esmaeel Sarvestani,[1] Gouren Zhang,[1] Evgeny Gorelov,[1,2] and Eva Pavarini[1,3,4]
[1]*Institute for Advanced Simulation, Forschungszentrum Jülich, 52425 Jülich, Germany*
[2]*European XFEL GmbH, Holzkoppel 4, 22869 Schenefeld, Germany*
[3]*JARA High-Performance Computing, RWTH Aachen University, 52062 Aachen, Germany*
[4]*JARA FIT, RWTH Aachen University, 52062 Aachen, Germany*

(Received 21 July 2017; revised manuscript received 10 January 2018; published 21 February 2018)

By using the local-density approximation + dynamical mean-field theory approach, we study the low-energy electronic properties and the optical conductivity of the layered ruthenates Sr_2RuO_4 and $Sr_3Ru_2O_7$. We study the interplay of spin-orbit, crystal-field, and Coulomb interactions, including the tetragonal terms of the Coulomb tensor. We show that the spin-orbit interaction is multifaced; depending on the parameter regime, filling, and temperature, it can either enhance or reduce the effective strength of correlations. We compare the results based on the two common approximations for the screened Coulomb parameters, the constrained random-phase approximation (cRPA) and the constrained local-density approximation. We show that the experimental Drude peak is better reproduced by the cRPA parameters, hinting to relatively small mass renormalizations. We find that including the spin-orbit interaction is, however, important, for a realistic description. We show that Coulomb terms with tetragonal D_{4h} symmetry have a strong effect on the mass-enhancement anisotropy, but they do not affect sizably the total spectral function or the in-plane conductivity.

DOI: 10.1103/PhysRevB.97.085141

I. INTRODUCTION

The Ruddlesden-Popper perovskites Sr_2RuO_4 and $Sr_3Ru_2O_7$ have exceptional electronic and magnetic properties, the first system being a possible realization of a p-wave superconductor [1–3] and the second displaying signatures of quantum-critical phenomena and nematic fluid behavior [4–6]. They are built of tetragonally elongated RuO_6 octahedra forming layers; the latter repeat along the **c** axis, separated by a distance and alternately shifted parallel to the **ab** plane; in Sr_2RuO_4 the octahedra form single-layer and in $Sr_3Ru_2O_7$ (Fig. 1) double-layer blocks. Due to their remarkable properties, these materials have been studied for decades [1–42].

Theoretically, the Ruddlesden-Popper ruthenates are especially intriguing because several competing interactions have similar strength. In such a situation it can become a challenge to disentangle the key mechanisms from the rest; indeed, our understanding of these materials was revised various times in the last decades. Due to the perovskite structure, the low-energy states have mostly Ru $4d$ t_{2g} character, with nominal configuration t_{2g}^4; the tetragonal (D_{4h}) distortion splits the t_{2g} states into a lower-energy xy singlet and a higher-energy (xz, yz) doublet; the crystal-field splitting $\varepsilon_{\rm CF} = \varepsilon_{xz/yz} - \varepsilon_{xy}$ is small, however. The layered structure yields rather different bandwidths for the xy and (xz, yz) electrons, with $W_{xy} > W_{xz/yz}$. As first guess, one could naively think that $4d$ systems of this kind are already well described by density-functional theory in the local-density approximation. Ruthenates, however, surprise in many ways. Already early calculations based on dynamical mean-field theory suggested that they should be regarded as correlated systems [7]. Recent *ab initio* estimates of the average screened Coulomb repulsion [8,9] show that the latter is comparable with the t_{2g} bandwidth, supporting the view of Sr ruthenates as correlated metals. Furthermore, experimentally, it has been found that when Sr is replaced by the isoelectronic Ca, the single-layered ruthenate becomes a Mott insulator below a critical temperature [11]. Later on, it was understood that the small crystal-field splitting $\varepsilon_{\rm CF}$ and the bandwidth mismatch $W_{xz}/W_{xy} \sim 0.5$ in Ca_2RuO_4 are key to explain this Mott transition [12,13]. Finally, in the last years it has been pointed out the remarkable role of the Hund's rule coupling J in enhancing the effective masses, thus making the ruthenates strongly correlated. This led to reclassify these systems as Hund's rather than Mott's metals [14]. Furthermore, an incoherent regime with quasilinear dependence of the scattering rate was identified [8]. Experimentally, sizable effective masses have been reported in Sr_2RuO_4 [3,15–17], and even larger in $Sr_3Ru_2O_7$ [18,19]. All these works have clarified essential aspects of the physics of the ruthenates, but others remain not fully understood, in particular, the effect of two interactions, the spin-orbit coupling and of tetragonal Coulomb terms, small but comparable with the crystal-field splitting and the hopping integrals.

It has been shown that already at the level of density-functional theory in the local-density approximation (LDA), the spin-orbit (SO) interaction plays a key role at the Fermi surface [20–22]. Accounting for the spin-orbit interaction within material-specific many-body models has been theoretically a challenge for a long time, in particular due to the infamous sign problem of quantum Monte Carlo (QMC) solvers for dynamical mean-field theory. Recently, we have generalized the continuous-time interaction-expansion (CT-INT) QMC solver to Hamiltonians of any symmetry, including the spin-

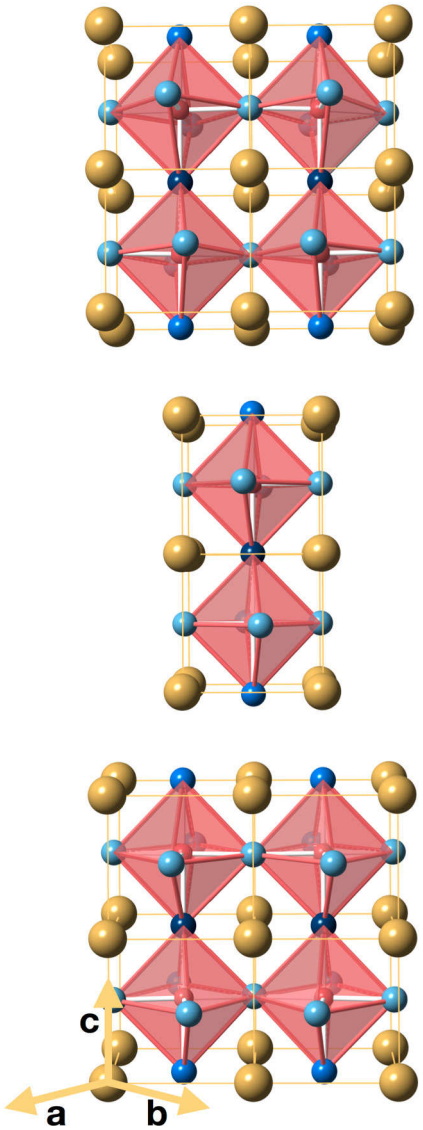

FIG. 1. The crystal structure of the double-layered ruthenate $Sr_3Ru_2O_7$. The RuO_6 octahedra forming the layers are slightly elongated and the cubic Sr cages slightly compressed along the **c** direction.

orbit interaction and general Coulomb vertex; in the cases we studied, we could improve computational efficiency via appropriated basis choices [23,24]; the sign problem remains manageable in all calculations we performed so far. By using this approach, we have shown that, for a proper description of the Fermi surface of Sr_2RuO_4 it is necessary to include the rotationally invariant [O(3)-symmetry] part of the Coulomb interaction plus the spin-orbit interaction. This is not sufficient, however. Small Coulomb terms with tetragonal (D_{4h}) symmetry [23] turn out to be essential. The natural question that arises is if these effects and their interplay are crucial only at the Fermi surface, where the right symmetry is key, or if they also appear in different properties and at higher energies, and can be detected in other types of experiments. In that respect, photoemission spectra, effective-mass measurements, and optical conductivity experiments are particularly important because they are typically used in comparing theory and experiments, and in particular to estimate the actual strength of the Coulomb terms or the validity of a given method and approximation.

In this paper, we thus reanalyze the correlated electronic structure of single- and double-layered ruthenates in the light of these new insights. We do this treating on the same footing and within the same calculation scheme all relevant competing interactions: the crystal-field splitting, the hopping integrals, spin-orbit interaction, and the Coulomb vertex, including low-symmetry terms with tetragonal (D_{4h}) symmetry. In particular, we examine low- and intermediate-energy properties such as effective masses and lifetimes, t_{2g} spectral functions, and optical conductivity. In addition, we compare results obtained with screened Coulomb parameters determined via the constrained random-phase approximation (cRPA) [8], which often underestimates the Coulomb parameters, and the constrained local-density approximation approach (cLDA) [9], which typically overestimates the Coulomb parameters, in order to identify which of these two typically adopted schemes yields more realistic values for layered ruthenates.

The paper is organized as follows. In Sec. II we describe the model and the approach we adopt, the LDA+DMFT method. In particular, we discuss how we deal with the spin-orbit terms using the continuous-time interaction-expansion quantum Monte Carlo method in a t_{2g} Wannier basis, and how we calculate the optical conductivity tensor. In Sec. III we present the results. For O(3)-symmetric Coulomb tensor, cRPA parameters and without spin-orbit coupling our results are in line with previous works [8,23,25]. We discuss how the effective masses are modified by the spin-orbit interaction, and how the nonspherical Coulomb terms affect the effective-mass orbital anisotropy. We show that in order to describe the optical conductivity measurements it is important to account for the spin-orbit interaction. We show that in average quantities (e.g., the total spectral function) the effects of Coulomb tetragonal terms are minor. They are, however, very important for the mass-enhancement anisotropy, determining an orbital-dependent band narrowing [31], and for the out-of-plane conductivity. We show that overall the cRPA parameters yield results in better agreement with currently available optical conductivity experiments and reported effective masses; the proper description of effective-mass anisotropy improves, however, if we explicitly account also for D_{4h} Coulomb terms. In Sec. IV we give our conclusions. Technical details of the calculations are explained in the Appendices.

II. MODEL AND METHOD

In order to calculate the electronic and transport properties of layered ruthenates, we use the local-density approximation plus dynamical mean-field theory (LDA+DMFT) approach [43]. First, we calculate the electronic structure in the local-density approximation (LDA) by using the full-potential linearized augmented plane-wave method as implemented in WIEN2K code [44]. Then, via the maximally localized Wannier function method [45,46] and t_{2g} projectors, we construct localized t_{2g}-like Wannier functions centered at Ru atoms spanning the t_{2g} bands. Using these Wannier orbitals we build

the t_{2g} Hubbard Hamiltonian

$$H = -\sum_{ii'\sigma\sigma'}\sum_{mm'} t^{ii'}_{m\sigma,m'\sigma'}\, c^{\dagger}_{im\sigma}c_{i'm'\sigma'} + \frac{1}{2}\sum_{i\sigma\sigma'}\sum_{mm'pp'} U_{mm'pp'}c^{\dagger}_{im\sigma}c^{\dagger}_{im'\sigma'}c_{ip'\sigma'}c_{ip\sigma} - H_{\text{d.c.}}, \quad (1)$$

where $c_{im\sigma}$ ($c^{\dagger}_{im\sigma}$) annihilates (creates) an electron at lattice site i with spin $\sigma \in \{\uparrow, \downarrow\}$ and orbital quantum number $m \in \{xy, yz, xz\}$. The one-electron terms $-t^{ii'}_{mm'}$ yield hopping integrals ($i \neq i'$) and the crystal-field matrix ($i = i'$). We calculate the noninteracting Hamiltonian both without (LDA) and with (LDA+SO) spin-orbit interaction. For what concerns the second case, the onsite part of the spin-orbit term takes the form

$$H_{\text{SO}} = \sum_{i\mu}\sum_{m\sigma m'\sigma'} \lambda_{\mu}\varepsilon^{i\mu}_{m\sigma m'\sigma'}c^{\dagger}_{im\sigma}c_{im'\sigma'},$$

where $\mu = x, y, z$, and

$$\varepsilon^{i\mu}_{m\sigma m'\sigma'} = \langle m\sigma|s^{i}_{\mu}l^{i}_{\mu}|m'\sigma'\rangle.$$

We extract the spin-orbit couplings by comparing the LDA and LDA+SO Hamiltonians. By ordering the basis as $|xy\rangle_{\uparrow}, |yz\rangle_{\uparrow}, |xz\rangle_{\uparrow}, |xy\rangle_{\downarrow}, |yz\rangle_{\downarrow}, |xz\rangle_{\downarrow}$, the onsite crystal-field matrix $\varepsilon_{m\sigma,m'\sigma'} = -t^{ii}_{m\sigma,m'\sigma'}$ for Sr_2RuO_4 (Ru site symmetry D_{4h}) and $Sr_3Ru_2O_7$ (Ru site symmetry C_2) can be then expressed as

$$\varepsilon = \begin{pmatrix} \varepsilon_{xy} & 0 & 0 & 0 & \frac{\lambda_y}{2} & -\frac{i\lambda_x}{2} \\ 0 & \varepsilon_{yz} & \frac{\delta_z+i\lambda_z}{2} & -\frac{\lambda_y}{2} & 0 & 0 \\ 0 & \frac{\delta_z-i\lambda_z}{2} & \varepsilon_{xz} & \frac{i\lambda_x}{2} & 0 & 0 \\ 0 & -\frac{\lambda_y}{2} & -\frac{i\lambda_x}{2} & \varepsilon_{xy} & 0 & 0 \\ \frac{\lambda_y}{2} & 0 & 0 & 0 & \varepsilon_{yz} & \frac{\delta_z-i\lambda_z}{2} \\ \frac{i\lambda_x}{2} & 0 & 0 & 0 & \frac{\delta_z+i\lambda_z}{2} & \varepsilon_{xz} \end{pmatrix}.$$

The diagonal terms are ε_{xz}, ε_{yz}, and ε_{xy}, where $\varepsilon_{xy} = (\varepsilon_{xz} + \varepsilon_{yz})/2 - \varepsilon_{\text{CF}}$, and where ε_{CF} is the crystal-field splitting in the absence of spin-orbit interaction; the couplings λ_x and λ_y are the spin-orbit matrix elements between xy and xz/yz orbitals and λ_z between yz and xz orbitals. For Sr_2RuO_4, the system with space group $I4/mmm$ and in which the Ru site symmetry is D_{4h}, $\varepsilon_{xz} = \varepsilon_{yz}$, $\delta_z = 0$, and $\varepsilon_{\text{CF}} = 121$ meV; the tetragonal anisotropy of the spin-orbit couplings is small, i.e., the LDA values are $\lambda_x = \lambda_y = \lambda_{xy} = 100$ meV and $\lambda_z = 102$ meV. For $Sr_3Ru_2O_7$, the symmetry of Ru sites is in principle lower (space group $Ccca$ [47], Ru site symmetry C_2). In practice, however, the Ru site has C_4 symmetry with tiny C_2 distortions; the C_2 splitting, $\varepsilon_{xz} - \varepsilon_{yz} \sim 1$ meV, is negligible and the same is true for $\delta_z \sim 2$ meV. The spin-orbit couplings are close to the Sr_2RuO_4 values, with $\lambda_x - \lambda_y \sim 0$, so that in the discussion we can use as parameters the average $\lambda_{xy} = (\lambda_x + \lambda_y)/2$, and $\lambda_z = 106$ meV, $\lambda_{xy} = 102$ meV. The crystal-field splitting is $\varepsilon_{\text{CF}} = 109$ meV. In both systems we find that the spin-orbit interaction affects mostly the onsite elements of the Hamiltonian. The terms $U_{mm'p'p}$ are elements of the screened Coulomb interaction tensor. In the O(3)-symmetric case, these elements can be expressed as a function of the Slater integrals F_0, F_2, and F_4. For t_{2g} states, the essential terms [43] are the direct [$U_{mm'mm'} = U_{m,m'} = U - 2J(1 - \delta_{m,m'})$] and the exchange ($U_{mm'm'm} = J$) screened Coulomb interaction, the pair-hopping ($U_{mmm'm'} = J$) and the spin-flip term ($U_{mm'm'm} = J$). In these expressions we used the relations $U = F_0 + \frac{4}{49}(F_2 + F_4)$ and $J = \frac{1}{49}(3F_2 + \frac{20}{9}F_4)$, as appropriate for t_{2g} states [43]. For site symmetry D_{4h} or C_4, the number of independent Coulomb parameters increases to six. In this work we will discuss in particular the effect of $\Delta U = U_{xy,xy} - U_{xz,xz}$ and $\Delta U' = U_{xy,yz} - U_{xz,yz}$, the most important terms. For Sr_2RuO_4, as already mentioned, the essential Coulomb integrals have been estimated *ab initio* both via the cLDA [9] and the cRPA approaches [8]. The first estimate yields $U = 3.1$ eV and $J = 0.7$ eV and the latter $U = 2.3$ eV and $J = 0.4$ eV. For $Sr_3Ru_2O_7$, given the strong similarities between the two materials, in the lack of more specific estimates, we adopt the same values. The term $H_{\text{d.c.}}$ is the double-counting correction. For an O(3)-symmetric Coulomb interaction, $H_{\text{d.c.}}$ is a mere shift of the chemical potential; in the presence of low-symmetry Coulomb terms, the double-counting correction plays an important role. Here, we adopt the around-mean-field approximation for dealing with low-symmetry terms (the explicit form of $H_{\text{d.c.}}$ is derived in Appendix C); this approximation is particularly suited for studying strongly correlated metals which exhibit in LDA negligible orbital polarization, as it is the case for layered Sr ruthenates.

We solve the Hamiltonian (1) with DMFT using continuous-time interaction-expansion (CT-INT) quantum Monte Carlo [13,48,49], explicitly including the spin-orbit coupling [23]. We perform calculations with a 6×6 self-energy matrix $\Sigma_{m\sigma,m'\sigma'}(\omega)$ in spin-orbital space. More specifically, we use the general implementation of CT-INT presented in Ref. [13] and extended to explicitly include the spin-orbit (SO) interaction in the solver in Ref. [23]. The choice of the one-electron basis influences the sign problem and numerical efficiency, as we have previously shown for the case of low-symmetry perovskites in the absence of spin-orbit interaction [50]. Here, the LDA+DMFT calculations with SO coupling are performed in the basis $|\tilde{m}\rangle_{\sigma} = \hat{T}|m\rangle_{\sigma}$, where the unitary operator $\hat{T}$ is chosen such that the local imaginary-time Green function matrix is real; since $\hat{T}$ only changes the phases but does not mix orbitals, in the discussion we will rename for simplicity $|\tilde{m}\rangle_{\sigma}$ as $|m\rangle_{\sigma}$. For Sr_2RuO_4 (D_{4h} symmetry), the transformation merely amounts to an extra $(-1)^{\sigma}\pi/2$ phase for the $|xz\rangle_{\sigma}$ orbital; as it can be shown by using group theory (details are given in Appendix B), this is an exact procedure. For $Sr_3Ru_2O_7$ (C_2 symmetry), the xz and yz orbitals can in principle mix; however, since the Ru site has almost C_4 symmetry, as we already pointed out, the C_2 mixing is tiny and the optimal phase transformation is very close to the one for Sr_2RuO_4.

The conductivity tensor $\text{Re}\,\sigma_{\alpha\alpha'}(\omega)$ can be expressed as follows:

$$\text{Re}\,\sigma_{\alpha\alpha'}(\omega) = -\frac{\text{Im}\,\chi_{\alpha\alpha'}(\omega + i0^{+})}{\omega},$$

where the label $\alpha = a, b, c$ indicates the direction. We obtain

the current-current correlation function

$$\chi_{\alpha\alpha'}(i\omega_n) = \frac{\hbar e^2}{\beta V}\sum_{\mathbf{k}p} \mathrm{Tr}\, \xi^{\mathbf{k}}_{\alpha,\alpha'}(i\omega_n, i\nu_p),$$

$$\xi^{\mathbf{k}}_{\alpha,\alpha'}(i\omega_n, i\nu_p) = [\mathbf{v}^{\mathbf{k}}]_{\alpha}\, G_{\mathbf{k}}(i\omega_n + i\nu_p)\, [\mathbf{v}^{\mathbf{k}}]_{\alpha'}\, G_{\mathbf{k}}(i\nu_p)$$

on the Matsubara axis; hence, here ω_n are bosonic and ν_p fermionic Matsubara frequencies, V is the volume, $\beta = 1/k_B T$ the inverse temperature, and $G_{\mathbf{k}}(i\nu_p)$ the Green-function matrix. The trace (Tr in the formula) is over spin-orbital degrees of freedom. The elements $\mathbf{v}^{\mathbf{k}}_{m\sigma,m'\sigma'}$ of the velocity matrices $\mathbf{v}^{\mathbf{k}}$ are calculated in the same Wannier basis in which the LDA+DMFT calculations are performed. The point group of layered ruthenates includes inversion symmetry, hence, the one-electron part of the t_{2g} Hamiltonian is even in $\mathbf{k}$, $H^{-\mathbf{k}}_{m\sigma,m'\sigma'} = H^{\mathbf{k}}_{m\sigma,m'\sigma'}$, while the velocity matrix is odd, $\mathbf{v}^{-\mathbf{k}}_{m\sigma,m'\sigma'} = -\mathbf{v}^{\mathbf{k}}_{m\sigma,m'\sigma'}$; thus, the local-vertex contribution to the current-current response function, which involves sums over $\mathbf{k}$ of the velocity matrix times an even function, vanishes. We perform the analytic continuation on the conductivity directly by using the f-sum rule to calculate the normalization factor. We employ two different analytic continuation methods, the maximum entropy method [51] and the stochastic approach of Mishchenko [52], obtaining very similar results. Finally, to better analyze the results we additionally calculate the conductivity via a different approach. In the latter, we first obtain the self-energy on the real axis; to this end, we perform the analytic continuation of the auxiliary Green-function matrix $\tilde{G}(i\nu_p) = 1/[i\nu_p + \tilde{\mu} - \Sigma(i\nu_p)]$, where $\tilde{\mu}$ is fixed such that the number of electrons is $N_e = 4$; we obtain the real part of the Green function from the imaginary part by using the Kramers-Kronig relation. The conductivity is then obtained as

$$\mathrm{Re}\,\sigma_{\alpha\alpha'}(\omega) = \hbar e^2 \int d\omega' \frac{f(\omega+\omega') - f(\omega')}{\omega} T_{\alpha\alpha'}(\omega,\omega'),$$

where $f(\omega)$ is the Fermi function and

$$T_{\alpha\alpha'}(\omega,\omega') = \frac{\pi}{V}\sum_{\mathbf{k}} \mathrm{Tr}([\mathbf{v}^{\mathbf{k}}]_{\alpha} A(\mathbf{k},\omega+\omega')[\mathbf{v}^{\mathbf{k}}]_{\alpha'} A(\mathbf{k},\omega'))$$

is the transport function. The term $A(\mathbf{k},\omega')$ is the spectral-function matrix and the trace is always over the six spin-orbital degrees of freedom. We find that the results of the two approaches are overall very similar.

III. RESULTS

A. Spectral function and quasiparticle masses

Let us start by analyzing the total spectral function of Sr_2RuO_4. This is shown in Fig. 2 for the two sets of interaction parameters, the one obtained via cLDA and the one calculated via cRPA. The differences between the results for the two parameter sets appear mostly in the position of the lower Hubbard band and the low-energy properties. The comparison with available photoemission and x-ray absorption spectroscopy experiments [9,53–55] yields relatively good agreement in both cases, and, alone, does not allow a clear-cut discrimination between results obtained via the cRPA and the cLDA Coulomb parameter sets. The same conclusion can be reached for $Sr_3Ru_2O_7$ [54–57]. In order to determine which

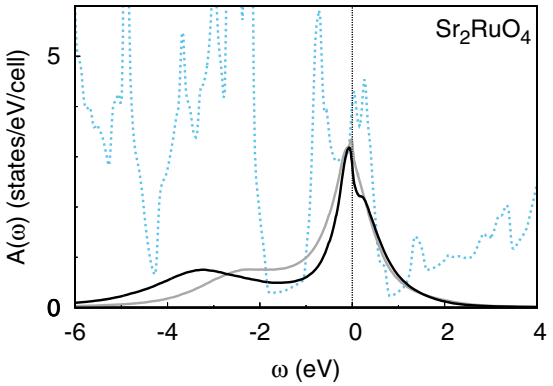

FIG. 2. Total t_{2g} spectral function of Sr_2RuO_4 calculated with the LDA+SO+DMFT approach for cLDA (dark line) and cRPA (light line) screened Coulomb parameters at temperature $T = 290$ K. The total LDA+SO density of states (all bands included) is also shown (dashed line). The chemical potential is set as the energy zero.

set of parameters is more realistic, we have to compare theory and experiments for additional properties; we will thus come back to this point at the end of the paper. In this section, we present results for both parameter sets.

Figure 3 shows the orbital-resolved mass enhancement $m^*/m \sim 1/Z$ and the quasiparticle scattering rate obtained as $\Gamma = -2Z\ \mathrm{Im}\,\Sigma(i\omega_0)$, in a wide range of temperature and for both Sr_2RuO_4 and $Sr_3Ru_2O_7$; these calculations have been performed using an O(3)-symmetric Coulomb vertex, with and without spin-orbit coupling. Previous calculations with cRPA parameters and no spin-orbit interaction [8] are in line with our results for the same case. It is important to point out that, switching from the cRPA to the cLDA parameter set, not only places the two systems sizably more inside the strong-correlation region, but it also yields a larger mass-enhancement anisotropy, defined as $R_M = (\frac{m^*}{m})_{xy}/(\frac{m^*}{m})_{xz/yz}$; we find that the latter increases by decreasing temperature. Figure 3 shows in addition that, on lowering the temperature down to 150 K, the

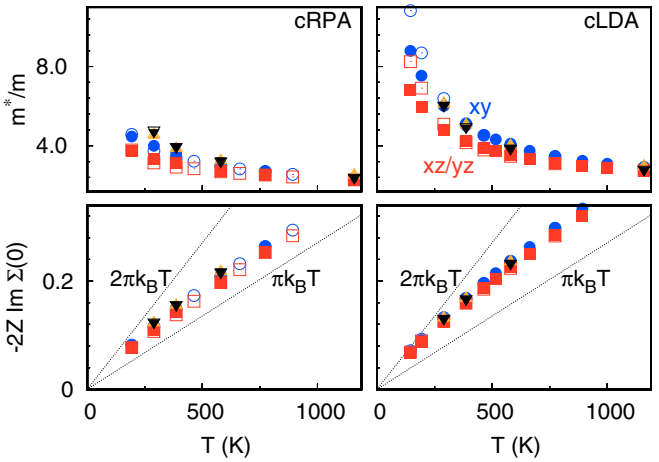

FIG. 3. Temperature dependence of the mass enhancement and of the effective quasiparticle scattering rate for Sr_2RuO_4. Full symbols: LDA+SO+DMFT results. Empty symbols: LDA+DMFT results. Squares: results for xz/yz orbitals. Circles: results for xy orbitals. Triangles: analogous results for $Sr_3Ru_2O_7$.

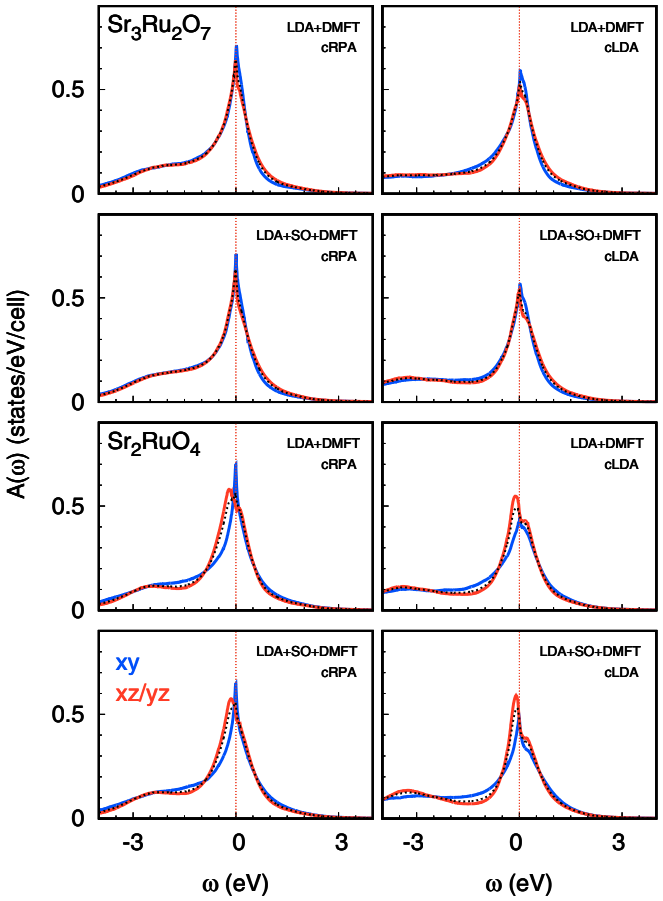

FIG. 4. Orbital-resolved spectral function per Ru and spin for Sr_2RuO_4 and $Sr_3Ru_2O_7$, calculated with LDA+DMFT and LDA+SO+DMFT at $T = 290$ K for the cRPA and the cLDA sets of interaction parameters. Dark line: xy orbital. Light line: xz/yz orbital. Black dots: average.

spin-orbit interaction reduces the effective masses but not so much R_M; the effect is stronger in the calculations based on the cLDA parameter set, for which U is larger and the atomic excited $S = 0$ multiplet is higher in energy. The scattering rates are, instead, similar in all the cases we consider since the parameter dependence of Z and Im $\Sigma(i\omega_0)$ largely compensate each other; for the same reason, they are also very similar in the single-layered compound Sr_2RuO_4 and in the double-layered system $Sr_3Ru_2O_7$.

Figure 4 shows the orbital-resolved spectral functions of Sr_2RuO_4 and $Sr_3Ru_2O_7$ at $T = 290$ K. For Sr_2RuO_4, the xy and xz/yz quasiparticle peaks are suppressed increasing the Coulomb interaction parameters from $(U, J) = (2.3, 0.4)$ eV to $(U, J) = (3.1, 0.7)$ eV. Switching on the spin-orbit interaction yields only small changes in the spectral functions. In the case of $Sr_3Ru_2O_7$, the spectral function is more orbital isotropic than in Sr_2RuO_4, both with and without spin-orbit interaction. This is reflected in the larger isotropy of the mass enhancement, that can be observed in Fig. 3. Finally, the effect of the spin-orbit interaction turns out to be different at low and intermediate energies; at intermediate energy, it slightly increases the bandwidth renormalization.

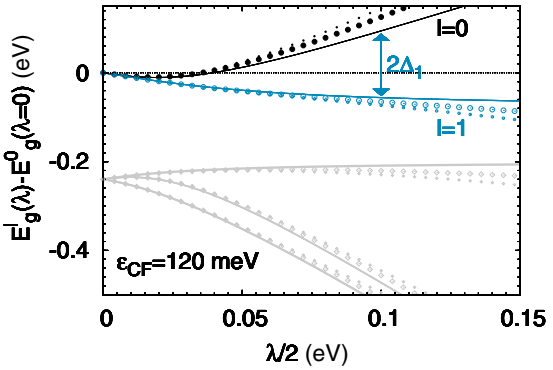

FIG. 5. Difference $\Delta E_g^l = E_g^l(\lambda) - E_g^0(0)$ in the atomic limit for $\lambda_{xy} = \lambda_z = \lambda$; here, $E_g^l(\lambda)$ is the gap associated with the lth eigenvalue of the atomic Hamiltonian for four electrons. Dark circles: $l = 0$ (ground state). The point at which the line crosses the zero moves to higher energy when ε_{CF} increases. Empty circles: excited doublet ($l = 1$). Gray symbols: next excited energies. Calculations were performed both for the cLDA (large symbols) and the cRPA (small symbols) parameters. Lines: results from the approximate formula described in the text.

Our results indicate that, indeed, in systems as the ruthenates, in which the strength of the spin-orbit coupling is comparable with the crystal-field splitting and the hopping integrals, the actual effect of the spin-orbit interaction is strongly dependent on details and the energy scales. This can be seen already in the atomic case, i.e., if we set the hopping integrals to zero. In such a limit we can calculate the gap analytically in the approximation in which only the lowest multiplet is taken into account, and couplings to higher-energy multiplets via the spin-orbit interaction are neglected (see Appendix D). This approximation is valid for spin-orbit couplings small compared to the Hund's rule coupling J, hence, it is slightly better suited for the cLDA than for the cRPA parameter set. In this limit, at $T = 0$ the atomic gap is given by $E_g^0 = E_0(N+1) + E_0(N-1) - 2E_0(N)$, where $E_0(N)$ is the energy of the ground state for N electrons. Furthermore, the energies of the many-body states in the lowest-energy multiplet can be expressed as $E_l(N) = E_{U,J}(N) + \varepsilon_l(N)$, where $E_{U,J}(N)$ depends only on U and J, and $\varepsilon_l(N)$ only on the spin-orbit couplings and the crystal-field splitting (see Appendix D). If we order the states such that $\varepsilon_{l+1} > \varepsilon_l$, the zero-temperature gap takes then the simple form

$$E_g^0 \sim U - 3J + \varepsilon_0(5) + \varepsilon_0(3) - 2\varepsilon_0(4),$$

where $\varepsilon_0(3) \sim 2\varepsilon_{CF}$ and

$$\varepsilon_0(5) \sim 4\varepsilon_{CF} - \frac{\left(\varepsilon_{CF} + \frac{\lambda_z}{2}\right) + \sqrt{\left(\varepsilon_{CF} + \frac{\lambda_z}{2}\right)^2 + 2\lambda_{xy}^2}}{2},$$

$$\varepsilon_0(4) \sim 2\varepsilon_{CF} + \frac{\left(\varepsilon_{CF} - \frac{\lambda_z}{2}\right) - \sqrt{\left(\varepsilon_{CF} - \frac{\lambda_z}{2}\right)^2 + 2\lambda_{xy}^2}}{2}.$$

Figure 5 shows the $T = 0$ atomic gap ($l = 0$ plots) for isotropic spin-orbit couplings. For realistic values of λ, the exact result, obtained by diagonalization of the full atomic Hamiltonian (circles), is close to that obtained from the approximate expression given above (full line). Figure 6 shows the exact $T = 0$ atomic gap for anisotropic spin-orbit couplings.

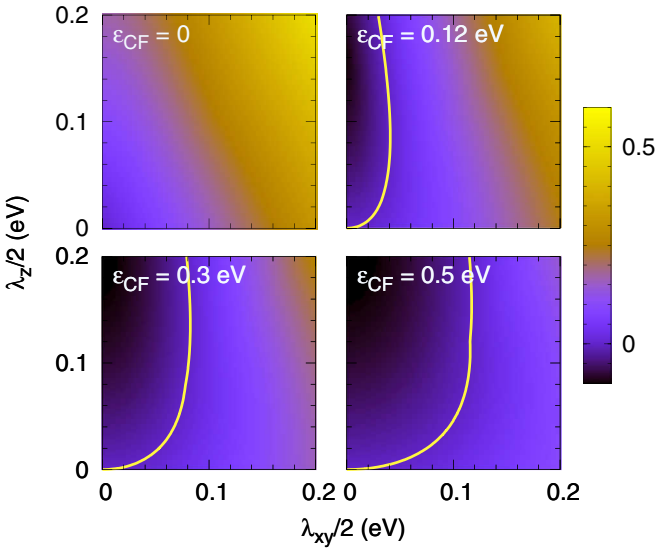

FIG. 6. The difference $\Delta E_g^0 = E_g^0(\lambda_z/2,\lambda_{xy}/2) - E_g^0(0,0)$, where $E_g^0(\lambda_z/2,\lambda_{xy}/2)$ is the $T = 0$ atomic limit gap in the presence of spin-orbit coupling. The four panels show the results for different values of the crystal-field splitting ε_{CF}. The light line shows the contour at which ΔE_g^0 changes sign from negative (left-hand side of the line) to positive (right-hand side). For $\varepsilon_{CF} = 0$ or in the large $\lambda = \lambda_z = \lambda_{xy}$ limit, $\Delta E_g^0 > 0$. The calculations have been performed for cLDA Coulomb parameters; results with cRPA parameters are similar.

As it can be seen in the figure, the spin-orbit interaction, depending on the parameters, either reduces or enhances the gap; in particular, when $\delta = \lambda_z - \lambda_{xy} > 0$, if the crystal field is large enough, the gap is reduced by the spin-orbit interaction, while if λ_{xy} is much larger than λ_z, the gap always increases. For crystal-field splitting and spin-orbit couplings corresponding to the cases of Sr_2RuO_4 and $Sr_3Ru_2O_7$, the parameters are very close to the contour line at which the sign changes, and $\delta \sim 2$–4 meV is small but positive. In addition, the three lower-energy $N = 4$ states are almost degenerate and thus form a quasitriplet, so that the effective degeneracy does not change; the energy difference between the ground state and the excited doublet is $\Delta_1 = E_1(N) - E_0(N) \sim 30$ meV for Sr_2RuO_4 and slightly larger in $Sr_3Ru_2O_7$, hence, the excited doublet is occupied for temperatures above 300 K. This can be inferred from Fig. 5, which shows, aside from the $T = 0$ gap, the differences $E_g^l(\lambda) - E_g^0(\lambda = 0)$ for $l > 0$, where $E_g^l = E_0(N+1) + E_0(N-1) - 2E_l(N)$ can be expressed as

$$E_g^l \sim U - 3J + \varepsilon_0(5) + \varepsilon_0(3) - 2\varepsilon_l(4) = E_g^0 - 2\Delta_l.$$

This yields the atomic gap when the excited state $E_l(N)$ is thermally populated, with weight $e^{-\Delta_l/k_BT}$. For $l = 1$,

$$\varepsilon_1(4) = 2\varepsilon_{CF} + \frac{\varepsilon_{CF} - \sqrt{\varepsilon_{CF}^2 + \lambda_{xy}^2}}{2}.$$

Figure 5 shows that Δ_1 increases with increasing spin-orbit coupling λ, and eventually becomes very large compared to k_BT. However, at room temperature, for a realistic $\lambda \sim 100$ meV, we have $\Delta_1 \sim k_BT$ and the atomic Green function poles corresponding to $l = 1$ have a sizable weight. Hence, already in the atomic limit, the effect of the spin-orbit interaction, both in terms of gap and effective degeneracy, is sensitive to the model details and temperature/energy scale.

Switching on the hopping integrals, in Sr_2RuO_4, both in the absence and presence of SO interaction the system shows negligible orbital polarization p, with $p = n_{xy} - (n_{xz} + n_{yz})/2$, despite the relative large crystal-field splitting. This happens because the kinetic energy gain compensates, due to the layered structure, the crystal-field energy loss coming from the occupation of the high-energy $N = 4$ multiplets. In order to understand this effect, it is sufficient to calculate the sum of the crystal-field energy loss and the superexchange energy gain per site for xy orbital order, in the small t/U limit. Let us consider a site and a cluster made of its four nearest neighbors; in the atomic limit, its energy is $10\varepsilon_{CF}$ when all sites are in the atomic ground state. The super-exchange energy gain yields

$$\Delta E^{OO_{xy}} \sim -\frac{4t_{xz}^2}{u},$$

where $u = 2/[1/U + 1/(U + 2J)]$ and $t_{xz} = t_{yz}$ the hopping among xz (or yz) orbitals on neighboring sites. This formula shows that switching on the hopping integrals stabilizes xy orbital order. The energy gain is small, however, because it involves excitations to doubly occupied states with average energy $U + J$. If the hopping integrals are large enough, however, a state corresponding to xy orbital order will become eventually degenerate with arrangements that involve an alternation of xy and xz orbitally ordered sites, as can be seen by diagonalizing exactly a two-site t_{2g} Hubbard model. The maximum superexchange energy gain associated to such a configuration is obtained for the ferromagnetic spin arrangement. It yields the energy difference

$$\Delta E^{OO_{xz/yz,xy}} \sim \frac{10}{4}\varepsilon_{CF} - \frac{4t_{xy}^2 + 2t_{xz}^2}{U - 3J}.$$

For sufficiently large hopping integrals, the superexchange energy gain is strong enough to overcome the energy loss due to the extra crystal-field energy. If the energy difference between configurations is comparable with k_BT, orbital fluctuations are strong and no orbital polarization is observed. This happens in the case of the ruthenates, where the kinetic and potential energy is large and the system remains metallic. For Sr_2RuO_4, the nearest-neighbor hoppings are, e.g., $t_{xy} \sim 379$ meV and $t_{xz} = t_{yz} \sim 292$ meV; in the limit in which the local Coulomb interaction is negligible (LDA), the positive crystal-field splitting is overcompensated by the smaller xz/yz bandwidth, yielding a tiny but slightly *negative* orbital polarization p. This remains true also in the presence of spin-orbit interaction.

Recently, it has been understood that the Hund's rule coupling can have a double-faced effect. Away from half-filling, on the one hand it reduces the atomic gap and on the other hand it decreases the effective Kondo energy scale [14], by effectively reducing the orbital degeneracy; the latter is crucial for the actual strength of correlations, as was shown in Ref. [58]. The effect of the spin-orbit coupling is, in that view, even more complex. As we have seen, already in the atomic limit, depending on the regimes, for filling $\frac{2}{3}$ (the case of ruthenates) it can either increase or decrease the gap (see Figs. 6 and 5); the same happens for filling $\frac{1}{3}$. Instead, at half-filling (t_{2g}^3 atomic configuration) the spin-orbit interaction always decreases the

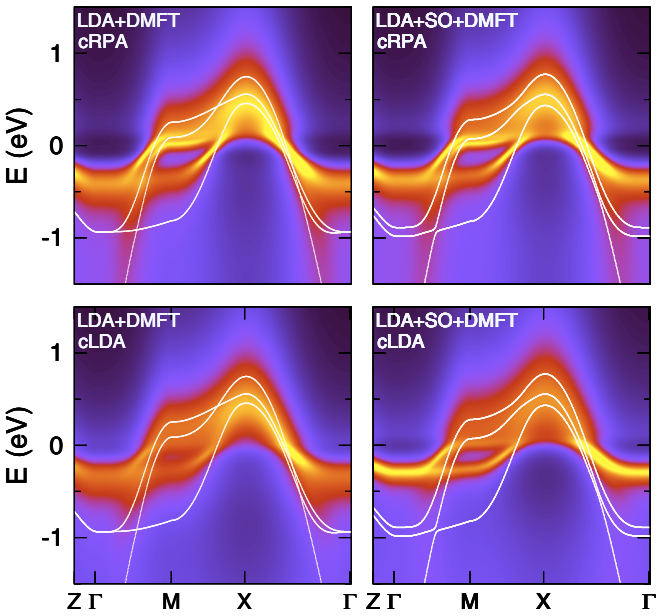

FIG. 7. Sr_2RuO_4: the LDA+DMFT (left panels) and LDA+SO+DMFT (right panels) band structure ($T = 290$ K). The light lines show the corresponding LDA and LDA+SO band structure.

gap since the energy of the $S = \frac{3}{2}$ ground multiplet is only modified by the spin-orbit interaction at second order in λ/J; here, we are assuming that, as typically the case for $3d$ and $4d$ systems, the ratio λ/J is small. Furthermore, in the absence of crystal-field interaction, the spin-orbit coupling decreases the effective degeneracy of many-body states. Thus, for a hypothetical t_{2g}^4 system in which the crystal-field splitting is negligible and the spin-orbit interaction is isotropic, everything else staying the same, λ, by itself, yields an enhancement of the atomic gap and a reduction of the effective degeneracy; in this situation, the spin-orbit interaction would favor in the atomic limit a ground-state multiplet with total angular momentum $j_t = 0$. If λ is, however, sufficiently large, higher-energy spin states mix with the ground multiplet and even the effect of the Hund's rule coupling is partially undone. Even more exotic cases could be obtained, e.g., in the hypothetical case in which the crystal-field splitting is finite and the spin-orbit anisotropy δ is large, so that the spin-orbit coupling sizably decreases the atomic gap. For the Sr ruthenates, where the crystal-field splitting is comparable to the spin-orbit interaction and the hopping integrals, as already observed, the effect is sensitive to parameters, energy scale, and the temperature. Figure 3 shows a reduction of the effective-mass enhancement down to 150 K, much smaller for cRPA than cLDA parameters. In Fig. 7 it may be seen that the difference in the spectral functions with and without spin-orbit interaction is small; at intermediate energies the correlated bands are, however, *slightly* more compressed in the presence of the spin-orbit interaction. At high temperature, the effect of spin-orbit interaction on masses and lifetimes becomes negligible.

B. Optical conductivity

The main theoretical results for the optical conductivity are shown in Fig. 8, where they are compared with experiments [59–69], and in Fig. 9. LDA+DMFT cRPA calculations with no spin-orbit interaction (Fig. 8, gray lines) are in line with previous similar calculations [60]. At high energy, the effect of increasing (U, J) from the cRPA to the cLDA values is minor; the differences appear mostly in the low- and intermediate-energy and temperature regimes. Figure 8 shows that already at 290 K, compared to the cLDA result, the cRPA static in-plane conductivity is sizably closer to the experimental value reported in Ref. [60], $\sigma_{\text{d.c.}} \sim 1.1 \times 10^4\ \Omega^{-1}\,\text{cm}^{-1}$. Switching on the spin-orbit coupling yields only small changes at this temperature; at a first glance, the effect of the spin-orbit interaction appears, however, qualitatively different in cRPA and cLDA results. The cRPA conductivity with spin-orbit coupling is merely shifted downwards with respect to the one obtained without spin-orbit term. In the case of cLDA calculations, instead, there is a transfer of spectral weight from intermediate energy scale to the low-energy region, which produces a small enhancement of the Drude peak. This apparently qualitative difference turns out to be a shift of energy

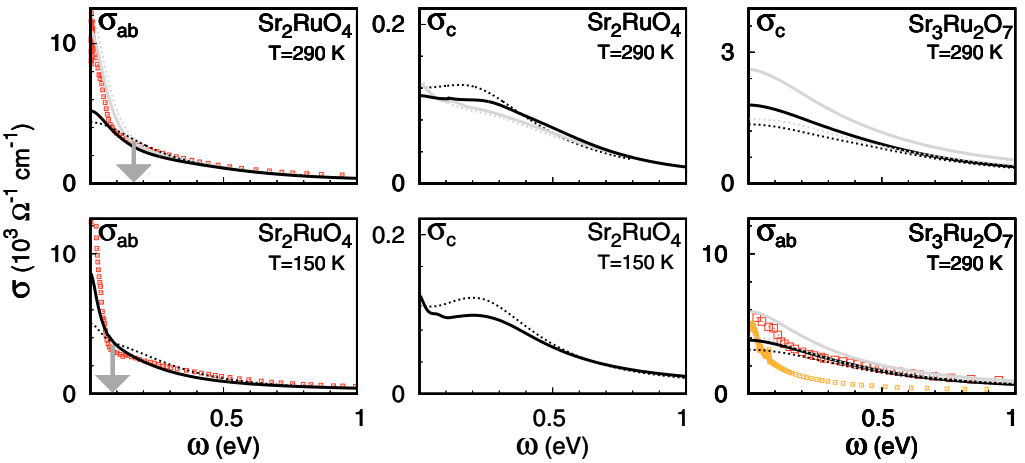

FIG. 8. Optical conductivity of Sr_2RuO_4 and $Sr_3Ru_2O_7$ calculated with LDA+DMFT (dashed lines) and LDA+SO+DMFT (full lines), for $(U, J) = (2.3, 0.4)$ eV (gray) and $(U, J) = (3.1, 0.7)$ eV (black). Experimental data are shown as squares. For Sr_2RuO_4, they are from Ref. [60], and for $Sr_3Ru_2O_7$ from Refs. [68] and (larger squares) [69]. The arrow indicates the frequency at which $\omega \sim 2\pi k_B T$.

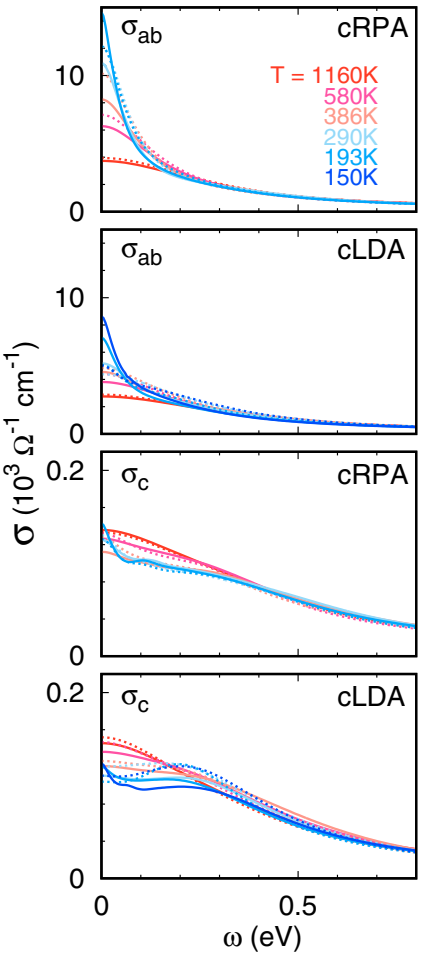

FIG. 9. Sr_2RuO_4: optical conductivity at different temperatures, calculated with LDA+DMFT (dots) and LDA+SO+DMFT (full lines), for cRPA and cLDA Coulomb parameters.

scale. Indeed, the effect of the spin-orbit interaction on the conductivity is strongly temperature dependent, as it can be seen by comparing the cLDA results at 290 and 150 K in Fig. 8, and more in detail the results for several temperatures shown in Fig. 9. At high enough temperatures, the spin-orbit interaction shifts downwards the static conductivity; on lowering the temperature, the Drude peak is progressively enhanced by the spin-orbit interaction, until eventually the curve with and without spin-orbit interaction cross. The crossing point takes place at lower temperatures/frequencies for the cRPA than for the cLDA parameters. When the temperature decreases down to 150 K, the calculations with spin-orbit interaction reproduce the experimental static conductivity ($\sigma_{\mathrm{d.c.}} \sim 3 \times 10^4\ \Omega^{-1}\,\mathrm{cm}^{-1}$ [60]) decisively better than those without spin-orbit interaction. Furthermore, the $2\pi k_B T$ foot (see Ref. [70] for theoretical discussion), emerging around $2\pi k_B T \sim 0.1$ eV in the 150-K experimental data, is also better reproduced. This can be seen both in Figs. 8 and 9. The effect of spin-orbit interaction is less dramatic for the **c**-axis conductivity $\sigma_c(\omega)$. In the case of $Sr_3Ru_2O_7$, we obtain a spin-orbit-driven enhancement of both the in-plane and out-of-plane conductivities. As for the single-layered compound, Fig. 8 shows that also for $Sr_3Ru_2O_7$ taking the spin-orbit interaction into account visibly improves the agreement with experiments [68,69], in particular at low frequencies. The figure additionally shows that the difference in magnitude between in-plane and out-of-plane conductivities decreases sizably with respect to Sr_2RuO_4, in line with previous observations [25]; for $Sr_3Ru_2O_7$, the value of $\sigma_c(\omega)$ is only a factor 3 smaller than $\sigma_{ab}(\omega)$.

Next, we analyze how the various effects influence the optical conductivity. For Sr_2RuO_4, in all cases (see Appendix A) the effect of the spin-orbit coupling on the velocities or the LDA Hamiltonian is minor for the in-plane conductivity; the same conclusion can be drawn for the effect the spin-orbit-induced off-diagonal elements of the self-energy. The main change is due to the diagonal elements of the self-energy itself. The out-of-plane conductivity $\sigma_c(\omega)$ behaves instead in a different way; the dominant effect arises from the velocity matrices; the next contribution is coming from the diagonal elements of the self-energy. Let us investigate the various contributions to the total conductivity. To this end, we split the transport function $T(\omega,\omega')$ into three terms, $T(\omega,\omega') = T_{\mathrm{intra}} + T_{\mathrm{inter}} + T_{\mathrm{mix}}$. The first term includes all intraorbital transitions. The interorbital term is defined as

$$T_{\mathrm{inter}} = \frac{2\pi}{V} \sum_{\mathbf{k},m\neq m'} \left[\mathbf{v}^{\mathbf{k}}_{m'm}\, A^{\mathbf{k}}_{mm}(\omega+\omega')\, \mathbf{v}^{\mathbf{k}}_{mm'}\, A^{\mathbf{k}}_{m'm'}(\omega)\right].$$

Finally, T_{mix} includes all remaining processes involving off-diagonal elements of the spectral function and/or the velocity matrix. In the case of Sr_2RuO_4, in the absence of spin-orbit interaction, the self-energy matrix is by symmetry orbital diagonal, and so is the local spectral function, hence the term T_{mix} yields a negligible contribution; furthermore, for the in-plane conductivity the intraorbital contributions dominate (see Appendix A) and xz/yz and xy contributions are comparable. Thus, the static in-plane conductivity is approximatively given by Allen's formula [70,71]

$$\sigma_{ab}(0) \sim \hbar e^2 \sum_m \frac{\gamma_m(0)}{2\,\mathrm{Im}\Sigma_{m,m}(0)},$$

where the function $\gamma_m(\varepsilon) = \frac{1}{V}\sum_{\mathbf{k}} |\mathbf{v}^{\mathbf{k}}_{mm}|^2 \delta(\varepsilon - \varepsilon_{m\mathbf{k}})$ is a weighted density of states. On lowering the temperature or decreasing (U,J) the imaginary part of the self-energy progressively decreases; this leads to an increase of the Drude peak. Switching on the spin-orbit interaction further decreases the imaginary part of the self-energy (see Fig. 10), while the effective quasiparticle lifetimes τ changes much less (see Fig. 3). At 150 K, the imaginary part of the self-energy is still larger (in absolute value) than $\pi k_B T$, and thus $1/\tau \sim 2\pi k_B T$, as Fig. 3 shows. We also find that the so-called incoherent regime [8,25], in which the scattering rate is almost linear in $k_B T$, extends to a large-temperature window for all cases (Fig. 3). An additional important effect of the spin-orbit interaction is that it gives rise to finite off-diagonal terms of the self-energy and spectral-function matrix, which in turn give rise to an important contribution from T_{mix}, in particular in the low-energy regime. At intermediate energy, these processes tend to decrease the final value, while at low frequencies, they have the opposite effect, i.e., they further contribute to the enhancement of the conductivity; this correspondingly enhances the foot at $\sim 2\pi k_B T$, signing the onset of the thermal regime [70]. The out-of-plane conductivity $\sigma_c(\omega)$ behaves very differently. We find that the two main terms come, in this case, from $T^{xz/yz}_{\mathrm{intra}}$ and $T^{xz,yz}_{\mathrm{inter}}$, and the latter dominates. When the

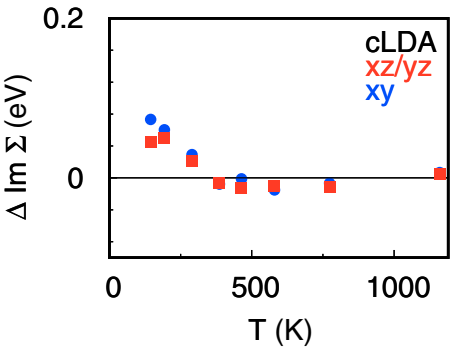

FIG. 10. Sr_2RuO_4: difference $\Delta\mathrm{Im}\Sigma = \mathrm{Im}\Sigma_{SO}(i\omega_0) - \mathrm{Im}\Sigma(i\omega_0)$ between the imaginary part of the self-energy at the first Matsubara frequency with and without SO interaction. For $|\mathrm{Im}\Sigma_{SO}(i\omega_0)| < |\mathrm{Im}\Sigma(i\omega_0)|$ the difference is positive. Squares: xz/yz orbitals. Circles: xy orbitals.

spin-orbit interaction is switched on, the first term decreases and the second increases.

Remarkably, the total in-plane and out-of-plane transport functions are very different; already in the noninteracting case, the in-plane term has a much larger weight at low energy than the out-of-plane terms. Increasing (U, J), the low-energy peak narrows, making the in-plane conductivity more sensitive to temperature changes. In the case of $Sr_3Ru_2O_7$, both in-plane and out-of-plane terms have a sizable weight at zero energy; thus, the strength of the temperature effect is comparable for $\sigma_{ab}(\omega)$ and $\sigma_c(\omega)$.

In conclusion, for Sr_2RuO_4, overall our LDA+DMFT results are qualitatively in line with experiments both for cRPA and cLDA parameters, i.e., both parameter sets correctly reproduce the main features (a Drude-type peak and a broad high-energy tail). The static in-plane conductivity appears, however, better reproduced by the cRPA parameter set than by cLDA values, which yield too short lifetimes. Even within cRPA results, however, the experimental Drude peak remains higher than the theoretical one unless we include explicitly the effects of the spin-orbit coupling. The latter enhances the zero-frequency peak at low enough temperatures. Indeed, LDA+SO+DMFT results are in remarkably better agreement with currently available experiments than LDA+DMFT spectra; this indicates that, contrarily to what is often assumed, the spin-orbit interaction is important for the realistic description of low-energy properties probed via optical conductivity experiments, and in particular the imaginary part of the self-energy. Instead, the quasiparticle lifetimes are much less affected by details, in line with typical approximations [72]. For $Sr_3Ru_2O_7$, we can similarly conclude that the spin-orbit interaction is necessary to reproduce correctly the experimental zero-frequency conductivity. Available experiments apparently differ among each other at finite frequency, however; further experimental investigation would be thus very important to finally settle the problem.

C. Effects of the tetragonal Coulomb terms

Up to here we have discussed results obtained with an O(3)-symmetric Coulomb vertex, the most commonly adopted approximation. Recently [23], we have shown that the D_{4h}-

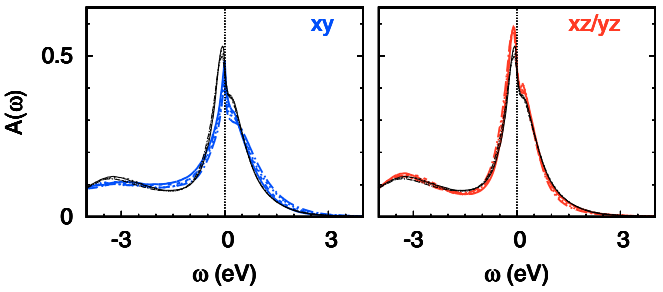

FIG. 11. Sr_2RuO_4: effect of ΔU on the orbital-resolved spectral function in states/eV/cell. Calculations are for $T = 290$ K, $(U, J) = (3.1, 0.7)$ eV, and with spin-orbit interaction. Full line: $\Delta U = 0$. Dashed curves with increasing dash level: $\Delta U = 0.15, 0.3, 0.45$ eV. Black lines: orbital average for each value of ΔU.

symmetric Coulomb terms strongly affect the shape of the Fermi surface of Sr_2RuO_4. Here, we analyze the effect of Coulomb anisotropy on the spectral function, the effective masses, and the optical conductivity. We first focus on the case of Sr_2RuO_4 and perform LDA+SO+DMFT calculations for a range of ΔU between 0 and 0.45 eV, and $0 \leqslant \Delta U' \leqslant \Delta U/3$; since the parameter $\Delta U'$ affects only weakly the results, here we will discuss mainly the effects of ΔU. The cRPA value is $\Delta U = 0.3$ eV, and lies in the middle of the range of values that we consider. There are at present no available cLDA-based results, but it is likely that the cLDA value of the Coulomb tetragonal anisotropy is slightly larger than the cRPA one; since (U, J) are about a factor 1.3–1.7 larger in cLDA, we can expect that, correspondingly, $\Delta U \sim 0.30$–0.45 eV in cLDA. The key results are shown in Figs. 11 and 12. Figure 11 shows that the average spectral functions do not change so much with increasing ΔU, while the orbital-dependent spectral functions exhibit a (small) weight transfer from the xy to the xz/yz states. More important, with increasing ΔU the effective mass of the xy orbital increases, while that of the xz/yz orbital decreases (Fig. 12); remarkably, the average mass enhancement remains instead almost constant. For the in-plane conductivity, although the relative contribution of different orbitals changes with

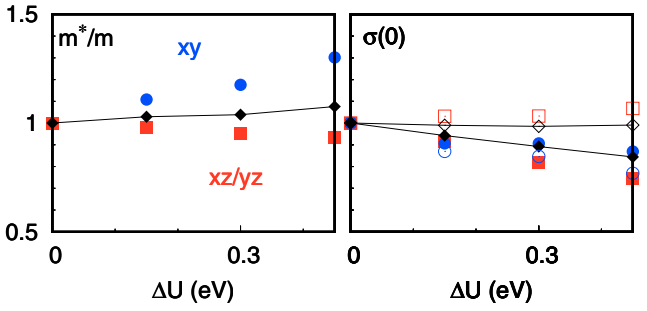

FIG. 12. Sr_2RuO_4: effect of ΔU on m^*/m (obtained from imaginary frequency data) and $\sigma(0)$, normalized to their $\Delta U = 0$ value. Squares: xz/yz intraorbital term. Circles: xy intraorbital term. Diamonds: orbital average. Empty symbols: $\sigma_{ab}(0)$. Filled symbols: $\sigma_c(0)$. Calculations are for cLDA parameters, $T = 290$ K, and with spin-orbit interaction. Results for cRPA parameters are similar but the effect weaker (e.g., for m^*/m we find a ∼10% instead of a ∼20% change for $\Delta U = 0.45$ eV).

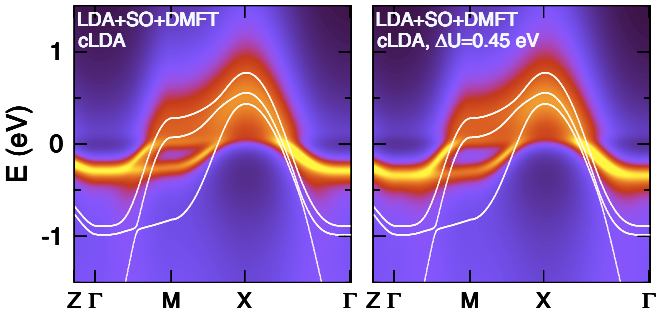

FIG. 13. Sr_2RuO_4: correlated band structure in the different cases ($T = 290$ K) with and without D_{4h} Coulomb terms. The latter increases the mass anisotropy.

increasing ΔU, the change in the total is very small, below 2% when ΔU increases from 0 to 0.45 eV. A larger effect can be seen in the out-of-plane conductivity, due to the fact that in this case are mostly the xz/yz terms (intraorbital and interorbital) that contribute. All together, this shows that the tetragonal Coulomb repulsion anisotropy has a large impact not only at the Fermi surface of Sr_2RuO_4 [23]. It reduces the out-of-plane conductivity and enhances visibly the effective-mass orbital anisotropy. Experimentally, relatively large mass anisotropy has been reported [3,15–17,31]. The effective masses and their anisotropy obtained in calculations with cRPA parameters are closer to reported experimental values than those obtained with cLDA parameters; the agreement between cRPA calculations and experiments tends to improve, however, when we account for the effect of D_{4h} Coulomb term. The correlated band structure with and without D_{4h} terms is shown in Fig. 13.

For the double-layered $Sr_3Ru_2O_7$ larger masses than for Sr_2RuO_4 have been reported [5,18,19,73]. Our cRPA-based results with O(3) Coulomb vertex already reproduce well this trend, as can be seen in Fig. 3; similar calculations yield analogous conclusions [25]. Furthermore, we find only a weak orbital dependence in the effective masses. The effect of the spin-orbit interaction is, down to 150 K, similar to what we find for the single-layered ruthenate. For what concerns Coulomb tetragonal terms, to the best of our knowledge, cRPA/cLDA estimates of ΔU are not yet available. Using the values of ΔU reported for Sr_2RuO_4, similar conclusions concerning the effects of tetragonal Coulomb terms hold for the double- and single-layered ruthenate. A negative ΔU would, on the other hand, reduce the effective-mass anisotropy or even, if sufficiently large, reverse its sign. Finally, we find that for both materials the effect of ΔU is much weaker not only in photoemission spectra, but also in the in-plane optical conductivity, i.e., in experiments in which an average of the contributions of the different orbitals is probed.

IV. CONCLUSIONS

In this work, we investigate the low-energy electronic properties and the optical conductivity of Sr_2RuO_4 and $Sr_3Ru_2O_7$. We adopt the LDA+DMFT approach and use a generalized continuous-time interaction-expansion quantum Monte Carlo solver. We study the effects of the spin-orbit interaction and of the tetragonal D_{4h} Coulomb terms, as well as their interplay with hopping integrals, crystal-field splitting, and O(3)-symmetric Coulomb interaction. In the first part of the paper we perform calculations with the O(3)-symmetric Coulomb vertex. We compare results obtained using different screened Coulomb parameter sets, one calculated via the constrained random-phase approximation approach [8] and the other via the constrained local-density approximation method [9]. This is important because it remains to date unclear which of these two approximated methods yields, in general, more realistic values of screened Coulomb parameters for LDA+DMFT calculations. The first method typically underestimates and the second method often overestimates the Coulomb parameters; this is in part due to the fact that in cRPA more screening channels are included [74]. The two approaches thus provide the interval in which realistic Coulomb parameters can vary. We show that, in the case of layered ruthenates, the cRPA-based results better describe currently available electronic transport data, in particular the static conductivity and the thermal regime. We show that, however, for a realistic description of the ruthenates, including the spin-orbit interaction is important. We show that in t_{2g} systems, the spin-orbit interaction can either increase or decrease the strength of correlation effects, depending on the parameters, the filling, and the energy scale. For the layered ruthenates, we find that down to 150 K the spin-orbit interaction partially reduces the mass enhancements and the low-frequency imaginary part of the self-energy, and thus enhances the optical conductivity. In the last part of our work we study the effects of the Coulomb tetragonal terms; in Sr_2RuO_4, the latter further enhance the ratio between the xy and xz/yz mass renormalization, improving the agreement with available experiments. Instead, the effects of the tetragonal Coulomb term ΔU is small in averaged quantities such as the in-plane conductivity and the total spectral function. These conclusions also apply to $Sr_3Ru_2O_7$; for the latter, material-specific estimates of ΔU are, to the best of our knowledge, not yet available, however. At a more general level, we conclude that both the low-symmetry screened Coulomb terms and the spin-orbit interaction can have a visible impact on low-energy properties. Thus, for systems in which they are comparable with other energy scales, these interactions should not be neglected even if they are difficult to be accounted for. This is in particular crucial when the aim is to identify the signatures of nonlocal physics, separating them from the effects which are already well described by the local self-energy approximation.

ACKNOWLEDGMENTS

Calculations have been done on the Jülich Blue Gene/Q. We acknowledge financial support from the Deutsche Forschungsgemeinschaft through the Research Training Group 1995.

APPENDIX A: ORBITAL-RESOLVED CONTRIBUTIONS TO $\sigma_{ab}(\omega)$

In this appendix, we analyze the various contributions to the in-plane and out-of-plane conductivity of Sr_2RuO_4. The conclusions for $Sr_3Ru_2O_7$ are similar (when taking the different unit cell into account). The results are shown in Fig. 14, where the original results of LDA+DMFT and LDA+SO+DMFT simulations are compared with several idealized calculations.

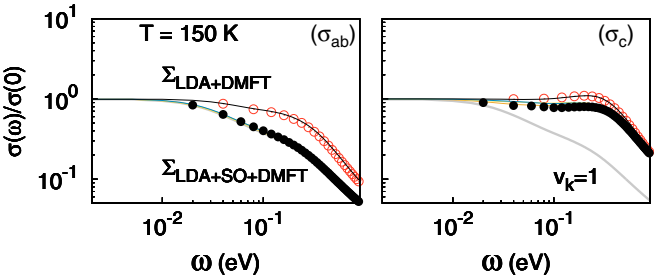

FIG. 14. Sr_2RuO_4 conductivity calculated with (filled circles) and without (empty circles) spin-orbit interaction ($T = 150$ K, cLDA parameters). Also shown are calculations in which (i) the velocity matrix elements are set to 1, (ii) the velocities with spin-orbit coupling are replaced by those without, (iii) the LDA Hamiltonian with spin orbit is replaced by the one without, (iv) the off-diagonal elements of the LDA+SO+DMFT self-energy matrix are neglected, and, finally, (v) the LDA+SO+DMFT self-energy is replaced by the LDA+DMFT self-energy (black line).

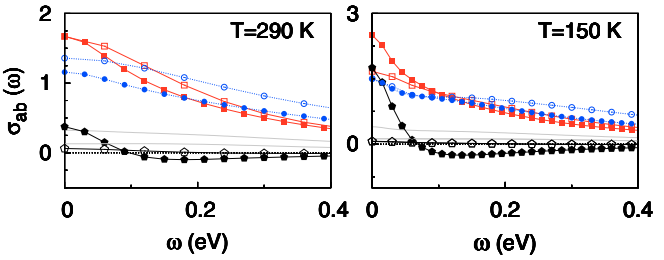

FIG. 15. Sr_2RuO_4: various contributions to the in-plane conductivity $\sigma_{ab}(\omega)$. Calculations are performed at 290 K (left) and 150 K (right), and for cLDA parameters. Intraband terms: squares (xz/yz) and circles (xy). Interband terms: gray lines. Rest: pentagons. Empty symbols: calculations without spin-orbit coupling. Full symbols: calculations with spin-orbit coupling. The conductivity is given in $10^3\ \Omega^{-1}\,\mathrm{cm}^{-1}$ units.

For the latter we use different approximations, consisting in replacing in the expression of the conductivity some terms with others. The figure shows, in particular, that the frequency dependence of $\sigma_{ab}(\omega)$ is not affected in a relevant way either by the velocities or by the off-diagonal elements of the self-energy. The main difference between the results with and without spin-orbit interactions comes instead from the diagonal elements of the self-energy themselves, and their modification due to the spin-orbit interaction. Remarkably, the conclusion is not the same for the out-of-plane conductivity $\sigma_c(\omega)$, for which the velocity element of matrix plays a key role. If the elements of matrices are set to one, the out-of-plane conductivity coincides with the in-plane conductivity. As for the in-plane conductivity, the effect of the spin-orbit coupling on the spectral function, instead, enters mostly via the diagonal terms of the self-energy. In Fig. 15 we show the in-plane contribution split into its most important components. Here, it may be seen that the effect of spin-orbit is twofold. First, it yields finite interorbital and mixed terms. Second, it enhances the contribution of the xz and yz intraorbital terms with respect to the contribution of the xy intraorbital term. This leads to an enhancement of the Drude peak and of the static conductivity, but also to a more pronounced foot at ∼0.1 eV.

APPENDIX B: SYMMETRY PROPERTIES OF LOCAL OPERATORS

Let us consider a Hermitian quadratic local operator $\hat{O}$ expressed in the t_{2g} basis $\{m\sigma\}$. This type of operator has a unique structure if the site symmetry is D_{4h}, C_4, or C_2. To derive this general form, we use the properties of the double groups associated with the point groups given above. Let us start with the group D_{4h}. In the absence of spin-orbit interaction, the irreducible representations of D_{4h} in which the cubic t_{2g} representation split are $b_{1g}\,(xy)$ and $e_g\,(xz,yz)$; this means that xy and (xz,yz) states do not couple, and the (xz,yz) states are degenerate, hence, only the $\hat{O}_{xy\sigma,xy\sigma} = o_{b_{1g}}$ and $\hat{O}_{xz\sigma,xz\sigma} = \hat{O}_{yz\sigma,yz\sigma} = o_{e_g}$ elements are nonzero. In the presence of spin-orbit interaction, the relevant irreducible representations are the Γ_6 and Γ_7, both twofold degenerate. The states $|7'\rangle_\sigma = |xy\rangle_\sigma$ and $|7''\rangle_\sigma = \frac{1}{\sqrt{2}}[|xz\rangle_\sigma + i(-1)^\sigma |yz\rangle_\sigma]$ are partner functions for the Γ_7 irreducible representation, while the states $|6\rangle_\sigma = \frac{1}{\sqrt{2}}[|xz\rangle_\sigma - i(-1)^\sigma |yz\rangle_\sigma]$ are partner functions for the Γ_6 irreducible representation; here, $(-1)^\sigma = -1$ for spin up and $(-1)^\sigma = +1$ for spin down. The states belonging to different irreducible representations or different rows/columns of the same irreducible representation do not couple, hence, the only elements which are not zero are $o'_7 = \hat{O}_{7'\sigma,7'\sigma}$, $o''_7 = o_{7''\sigma,7''\sigma}$, $o_7 = i\hat{O}_{7'\sigma,7''-\sigma}$, and $o_6 = \hat{O}_{6\sigma,6\sigma}$. By rotating back to the original basis, ordered as $|xy\rangle_\uparrow$, $|yz\rangle_\uparrow$, $|xz\rangle_\uparrow$, $|xy\rangle_\downarrow$, $|yz\rangle_\downarrow$, $|xz\rangle_\downarrow$, we find $\hat{O} = \hat{O}_0 + \hat{O}_1$, where the first part is diagonal:

$$\hat{O}_0 = \begin{pmatrix} o'_7 & 0 & 0 & 0 & 0 & 0 \\ 0 & \frac{o_6+o''_7}{2} & 0 & 0 & 0 & 0 \\ 0 & 0 & \frac{o_6+o''_7}{2} & 0 & 0 & 0 \\ 0 & 0 & 0 & o'_7 & 0 & 0 \\ 0 & 0 & 0 & 0 & \frac{o_6+o''_7}{2} & 0 \\ 0 & 0 & 0 & 0 & 0 & \frac{o_6+o''_7}{2} \end{pmatrix}.$$

The second term, the off-diagonal part, is zero in the absence of spin-orbit interaction. In the presence of spin-orbit interaction it takes the form

$$\hat{O}_1 = \begin{pmatrix} 0 & 0 & 0 & 0 & \frac{o_7}{\sqrt{2}} & \frac{-io_7}{\sqrt{2}} \\ 0 & 0 & \frac{i(o_7-o_6'')}{2} & \frac{-\overline{o_7}}{\sqrt{2}} & 0 & 0 \\ 0 & \overline{\frac{i(o_7-o_6'')}{2}} & 0 & \overline{\frac{-io_7}{\sqrt{2}}} & 0 & 0 \\ 0 & \frac{-o_7}{\sqrt{2}} & \frac{-io_7}{\sqrt{2}} & 0 & 0 & 0 \\ \frac{\overline{o_7}}{\sqrt{2}} & 0 & 0 & 0 & 0 & \overline{\frac{i(o_7-o_6'')}{2}} \\ \overline{\frac{-io_7}{\sqrt{2}}} & 0 & 0 & 0 & \frac{i(o_7-o_6'')}{2} & 0 \end{pmatrix}.$$

This shows that, in order to make real any D_{4h}-symmetric local operator of this type, it is sufficient to introduce an extra $(-1)^\sigma \pi/2$ phase for the $|xz\rangle_\sigma$ orbital. In the case of point group C_4, nothing changes; in the absence of spin orbit, the cubic t_{2g} split into $b\,(xy)$ and $e\,(xz, yz)$ irreducible representations, and a local operator has the same structure as in the D_{4h} case. In the C_2 case, however, the situation is more complex since there is only one spinor irreducible representation Γ^5. The corresponding matrix for a local object is given by $\hat{O} + \delta\hat{O}$, where $\hat{O} = \hat{O}_0 + \hat{O}_1$, provided that we replace $o_7' \to o_5'$, $o_6 \to o_5^6$, $o_7'' \to o_5''$, $o_7 \to o_5$. The additional term is

$$\delta\hat{O} = \begin{pmatrix} 0 & 0 & 0 & 0 & \frac{-\delta o_5}{\sqrt{2}} & \frac{-i\delta o_5}{\sqrt{2}} \\ 0 & \frac{-2\delta o_5^R}{2} & \frac{2i\delta o_5^I}{2} & \frac{\overline{\delta o_5}}{\sqrt{2}} & 0 & 0 \\ 0 & \frac{-2io_5^I}{2} & \frac{2\delta^R o_5^6}{2} & -\frac{\overline{i\delta o_5}}{\sqrt{2}} & 0 & 0 \\ 0 & \frac{\delta o_5}{\sqrt{2}} & \frac{-i\delta o_5}{\sqrt{2}} & 0 & 0 & 0 \\ \frac{-\overline{\delta o_5}}{\sqrt{2}} & 0 & 0 & 0 & \frac{-2\delta o_5^R}{2} & \frac{-2i\delta o_5^I}{2} \\ \frac{-\overline{i\delta o_5}}{\sqrt{2}} & 0 & 0 & 0 & \frac{2i\delta o_5^I}{2} & \frac{2\delta^R o_5^6}{2} \end{pmatrix}.$$

We find that for Ru sites the elements of $\delta\hat{O}$ are negligible in $Sr_3Ru_2O_7$, and that thus basically the same structure holds for a Ru-centered local operator as in Sr_2RuO_4.

APPENDIX C: HARTREE-FOCK LIMIT OF THE SELF-ENERGY AND DOUBLE-COUNTING CORRECTION

In the large-frequency limit, the DMFT self-energy equals the Hartree-Fock self-energy. The latter can be calculated from the Hartree-Fock Hamiltonian

$$\begin{aligned} H_{\mathrm{HF}} =& \frac{1}{2}\sum_{mp\sigma\sigma' m' p'} U_{mm' pp'}\left[\hat{n}_{mp}^{\sigma\sigma} n_{m'p'}^{\sigma'\sigma'} - \hat{n}_{mp'}^{\sigma\sigma'} n_{m'p}^{\sigma'\sigma}\right] \\ &+ \frac{1}{2}\sum_{mp\sigma\sigma' m' p'} U_{mm' pp'}\left[n_{mp}^{\sigma\sigma}\hat{n}_{m'p'}^{\sigma'\sigma'} - n_{mp'}^{\sigma\sigma'}\hat{n}_{m'p}^{\sigma'\sigma}\right] \\ &- \frac{1}{2}\sum_{mp\sigma\sigma' m' p'} U_{mm' pp'}\left[n_{mp}^{\sigma\sigma} n_{m'p'}^{\sigma'\sigma'} - n_{mp'}^{\sigma\sigma'} n_{m'p}^{\sigma'\sigma}\right], \end{aligned}$$

where $\hat{n}_{mm'}^{\sigma\sigma'}$ is an element of the density matrix. For the model specifically considered in this work, the essential terms correspond to an effective shift of the onsite parameters $\varepsilon_{\mathrm{CF}} \to \varepsilon_{\mathrm{CF}} + \Delta\varepsilon_{\mathrm{CF}}$, $\lambda_i \to \lambda_i + \Delta\lambda_i$, with

$$\Delta\varepsilon_{\mathrm{CF}} = \left[\frac{p}{2}(U - 5J) - \frac{\Delta U}{6}(n + p) - \frac{\Delta U'}{3}(n - p)\right]$$

and

$$\begin{aligned} \frac{\Delta\lambda_z}{2} &= -\,[U - 3J - \Delta U']n_{xz,yz}^{\sigma\sigma'}\,\delta_{\sigma,\sigma'}, \\ \frac{\Delta\lambda_{xy}^{xz/yz}}{2} &= -\,[U - 3J]n_{xy,xz/yz}^{\sigma\sigma'}\delta_{\sigma,-\sigma'}. \end{aligned}$$

In the formulas above the parameter $n = n_{xy} + n_{xz} + n_{yz} = 4$ is the number of electrons and the parameter $p = n_{xy} - (n_{xz} + n_{yz})/2$ is the orbital polarization; here, we have defined for simplicity $n_m = n_{mm}^{\uparrow\uparrow} + n_{mm}^{\downarrow\downarrow}$. We can now use these results to calculate the double-counting correction for the nonspherical terms. For metallic systems with negligible orbital polarization, it is reasonable to assume that LDA describes very well the average Coulomb interaction in the around mean-field approximation. This corresponds to the term

$$\begin{aligned} H^{\mathrm{HF}} =& \frac{n}{6}\sum_{m\sigma\sigma' m'} \hat{n}_{mm}^{\sigma\sigma}[U_{mm'mm'} - U_{mm'm'm}\delta_{\sigma,\sigma'}] \\ &-\left(\frac{n}{6}\right)^2\frac{1}{2}\sum_{mp\sigma\sigma' m' p'}[U_{mm'mm'} - U_{mm'm'm}\delta_{\sigma,\sigma'}]. \end{aligned}$$

Hence, after adding up all O(3)-symmetric terms in a chemical potential $\delta\mu$, we have, for the terms explicitly discussed in this work, we obtain the expression

$$H_{\mathrm{d.c.}}^{\mathrm{AMF}} = \delta\mu\;\hat{n} + \frac{n}{6}[\Delta U + 2\Delta U']\sum_\sigma \hat{n}_{xy}^\sigma.$$

APPENDIX D: ATOMIC MULTIPLETS AND THEIR ENERGIES

In the atomic limit, the ground-state multiplets in the presence of the spin-orbit interaction are listed below; we neglect intermultiplet couplings due to the spin-orbit interaction. This

TABLE I. The $N = 4$ and 5 ground multiplets in the presence of crystal field and spin-orbit interaction, in the case $\lambda_{xy} = \lambda_x = \lambda_y$. For convenience, we have introduced the $N = 4$ states $|m,\sigma_1+\sigma_2\rangle = \frac{1}{\sqrt{2(1+|\sigma_1+\sigma_2|)}}[c^\dagger_{m_1\sigma_1}c^\dagger_{m_2\sigma_2} + c^\dagger_{m_1\sigma_2}c^\dagger_{m_2\sigma_1}]c^\dagger_{m\uparrow}c^\dagger_{m\downarrow}|0\rangle$, and the $N = 5$ states $|\tilde{m},\sigma\rangle = c^\dagger_{\tilde{m},\sigma}c^\dagger_{m_2\uparrow}c^\dagger_{m_2\downarrow}c^\dagger_{m_1\uparrow}c^\dagger_{m_1\downarrow}|0\rangle$. The states with $N = 2$ and 1 electrons can be obtained from those given in the table above by using particle-hole symmetry. The coefficients α_{2i+1} and α_{2i+2} ($i = 0,1,2$) are such that $\alpha^2_{2i+1} + \alpha^2_{2i+2} = 1$, while $\alpha^2_{2i+1} = \frac{b^2_{2i+1}\lambda^2_{xy}}{(a_{2i+1}-\sqrt{a^2_{2i+1}+b^2_{2i+1}\lambda^2_{xy}})^2+b^2_{2i+1}\lambda^2_{xy}}$, where $a_1 = \varepsilon_{\rm CF}$, $a_3 = \varepsilon_{\rm CF} - \lambda_z$, and $a_5 = -\varepsilon_{\rm CF} - \lambda_z/2$, and $b_1 = 1$, $b_3 = b_5 = \sqrt{2}$.

$\lvert N;\alpha\rangle$	$E_l(N) = E_{U,J}(N) + \varepsilon_l(N)$
$\lvert 4;b,2\sigma\rangle = \frac{1}{\sqrt{2}}[\lvert xz,2\sigma\rangle + 2i\sigma\lvert yz,2\sigma\rangle]$	$6U - 13J + 3\varepsilon_{\rm CF} + \frac{\lambda_z}{2}$
$\lvert 4;a_{2g}\rangle = \frac{1}{2}[\lvert xz,-1\rangle + i\lvert yz,-1\rangle - \lvert xz,+1\rangle + i\lvert yz,+1\rangle]$	$6U - 13J + 3\varepsilon_{\rm CF} - \frac{\lambda_z}{2}$
$\lvert 4;e''_g a\rangle = \alpha_1\lvert xy,+1\rangle + \frac{\alpha_2}{\sqrt{2}}[\lvert xz,0\rangle + i\lvert yz,0\rangle]$	$6U - 13J + 2\varepsilon_{\rm CF} + \frac{1}{2}\left[\varepsilon_{\rm CF} + \sqrt{\varepsilon^2_{\rm CF} + \lambda^2_{xy}}\right]$
$\lvert 4;e''_g b\rangle = \alpha_1\lvert xy,-1\rangle + \frac{\alpha_2}{\sqrt{2}}[\lvert xz,0\rangle - i\lvert yz,0\rangle]$	$6U - 13J + 2\varepsilon_{\rm CF} + \frac{1}{2}\left[\varepsilon_{\rm CF} + \sqrt{\varepsilon^2_{\rm CF} + \lambda^2_{xy}}\right]$
$\lvert 4;e'_g a\rangle = \alpha_2\lvert xy,+1\rangle - \frac{\alpha_1}{\sqrt{2}}[\lvert xz,0\rangle + i\lvert yz,0\rangle]$	$6U - 13J + 2\varepsilon_{\rm CF} + \frac{1}{2}\left[\varepsilon_{\rm CF} - \sqrt{\varepsilon^2_{\rm CF} + \lambda^2_{xy}}\right]$
$\lvert 4;e'_g b\rangle = \alpha_2\lvert xy,-1\rangle - \frac{\alpha_1}{\sqrt{2}}[\lvert xz,0\rangle - i\lvert yz,0\rangle]$	$6U - 13J + 2\varepsilon_{\rm CF} + \frac{1}{2}\left[\varepsilon_{\rm CF} - \sqrt{\varepsilon^2_{\rm CF} + \lambda^2_{xy}}\right]$
$\lvert 4;a''_{1g}\rangle = \alpha_3\lvert xy,0\rangle + \frac{\alpha_4}{2}[\lvert xz,-1\rangle + i\lvert yz,-1\rangle + \lvert xz,+1\rangle - i\lvert yz,+1\rangle]$	$6U - 13J + 2\varepsilon_{\rm CF} + \frac{1}{2}\left[\varepsilon_{\rm CF} - \frac{\lambda_z}{2} + \sqrt{\left(\varepsilon_{\rm CF} - \frac{\lambda_z}{2}\right)^2 + 2\lambda^2_{xy}}\right]$
$\lvert 4;a'_{1g}\rangle = \alpha_4\lvert xy,0\rangle - \frac{\alpha_3}{2}[\lvert xz,-1\rangle + i\lvert yz,-1\rangle + \lvert xz,+1\rangle - i\lvert yz,+1\rangle]$	$6U - 13J + 2\varepsilon_{\rm CF} + \frac{1}{2}\left[\varepsilon_{\rm CF} - \frac{\lambda_z}{2} - \sqrt{\left(\varepsilon_{\rm CF} - \frac{\lambda_z}{2}\right)^2 + 2\lambda^2_{xy}}\right]$
$\lvert 5;\Gamma_6,\sigma\rangle = \frac{1}{\sqrt{2}}[\lvert \tilde{x}z,\sigma\rangle + 2i\sigma\lvert \tilde{y}z,\sigma\rangle]$	$10U - 20J + 3\varepsilon_{\rm CF} + \frac{\lambda_z}{2}$
$\lvert 5;\Gamma''_7,\sigma\rangle = \alpha_5\lvert \tilde{x}y,\sigma\rangle + \frac{\alpha_6}{\sqrt{2}}[\lvert \tilde{x}z,-\sigma\rangle - 2i\sigma\lvert \tilde{y}z,-\sigma\rangle]$	$10U - 20J + 4\varepsilon_{\rm CF} + \frac{1}{2}\left[-\varepsilon_{\rm CF} - \frac{\lambda_z}{2} + \sqrt{\left(\varepsilon_{\rm CF} + \frac{\lambda_z}{2}\right)^2 + 2\lambda^2_{xy}}\right]$
$\lvert 5;\Gamma'_7,\sigma\rangle = \alpha_6\lvert \tilde{x}y,\sigma\rangle - \frac{\alpha_5}{\sqrt{2}}[\lvert \tilde{x}z,-\sigma\rangle - 2i\sigma\lvert \tilde{y}z,-\sigma\rangle]$	$10U - 20J + 4\varepsilon_{\rm CF} + \frac{1}{2}\left[-\varepsilon_{\rm CF} - \frac{\lambda_z}{2} - \sqrt{\left(\varepsilon_{\rm CF} + \frac{\lambda_z}{2}\right)^2 + 2\lambda^2_{xy}}\right]$

approximation is valid for small λ/J. The next multiplet has $S = 0$ and it is, neglecting spin-orbit effects, higher in energy of $2J$. The states with $N = 3$ electrons do not split when intermultiplet couplings due to the spin-orbit interaction are neglected; they have therefore energy $3U - 9J$ (ground multiplet), $3U - 6J$, and $3U - 4J$. The complete list of states for $\lambda = 0$ can be found in Ref. [24]. The $N = 4$ and 5 states are given in Table I. The states for $N = 2$ and 1 can be obtained from those given in the table for $N = 1$ and 5 by using particle-hole symmetry.

[1] T. M. Rice and M. Sigrist, J. Phys.: Condens. Matter **7**, L643 (1995).

[2] K. Ishida, H. Mukuda, Y. Kitaoka, K. Asayama, Z. Q. Mao, Y. Mori, and Y. Maeno, Nature (London) **396**, 658 (1998).

[3] A. P. Mackenzie and Y. Maeno, Rev. Mod. Phys. **75**, 657 (2003).

[4] R. S. Perry, L. M. Galvin, S. A. Grigera, L. Capogna, A. J. Schofield, A. P. Mackenzie, M. Chiao, S. R. Julian, S. Ikeda, S. Nakatsuji *et al.*, Phys. Rev. Lett. **86**, 2661 (2001).

[5] R. A. Borzi, S. A. Grigera, R. S. Perry, N. Kikugawa, K. Kitagawa, Y. Maeno, and A. P. Mackenzie, Phys. Rev. Lett. **92**, 216403 (2004).

[6] S. Grigera, R. S. Perry, A. J. Schofield, M. Chiao, S. R. Julian, G. G. Lonzarich, S. I. Ikeda, Y. Maeno, A. J. Millis, and A. P. Mackenzie, Science **294**, 329 (2001).

[7] A. Liebsch and A. Lichtenstein, Phys. Rev. Lett. **84**, 1591 (2000).

[8] J. Mravlje, M. Aichhorn, T. Miyake, K. Haule, G. Kotliar, and A. Georges, Phys. Rev. Lett. **106**, 096401 (2011). In this work, at high temperature, a somewhat larger orbital dependence of the scattering rate is found; this is perhaps due to the different procedure used by the authors (Z is apparently calculated from Matsubara frequency data, and $\mathrm{Im}\Sigma(0)$ from real axis data).

[9] Z. V. Pchelkina, I. A. Nekrasov, T. Pruschke, A. Sekiyama, S. Suga, V. I. Anisimov, and D. Vollhardt, Phys. Rev. B **75**, 035122 (2007).

[10] Z. Wang, D. Walkup, P. Derry, T. Scaffidi, M. Rak, S. Vig, A. Kogar, I. Zeljkovic, A. Husain, L. H. Santos *et al.*, Nat. Phys. **13**, 799 (2017).

[11] C. S. Alexander, G. Cao, V. Dobrosavljevic, S. McCall, J. E. Crow, E. Lochner, and R. P. Guertin, Phys. Rev. B **60**, R8422 (1999).

[12] A. Liebsch and H. Ishida, Phys. Rev. Lett. **98**, 216403 (2007).

[13] E. Gorelov, M. Karolak, T. O. Wehling, F. Lechermann, A. I. Lichtenstein, and E. Pavarini, Phys. Rev. Lett. **104**, 226401 (2010).

[14] L. de'Medici, J. Mravlje, and A. Georges, Phys. Rev. Lett. **107**, 256401 (2011).

[15] C. Bergemann, A. P. Mackenzie, S. R. Julian, D. Forsythe, and E. Ohmichi, Adv. Phys. **52**, 639 (2003).

[16] N. J. C. Ingle, K. M. Shen, F. Baumberger, W. Meevasana, D. H. Lu, Z.-X. Shen, S. Nakatsuji, Z. Q. Mao, Y. Maeno, T. Kimura, and Y. Tokura, Phys. Rev. B **72**, 205114 (2005).

[17] T. E. Kidd, T. Valla, A. V. Fedorov, P. D. Johnson, R. J. Cava, and M. K. Haas, Phys. Rev. Lett. **94**, 107003 (2005).

[18] J. Lee, M. P. Allan, M. A. Wang, J. Farrell, S. A. Grigera, F. Baumberger, J. C. Davis, and A. P. Mackenzie, Nat. Phys. **5**, 800 (2009).

[19] M. P. Allan, A. Tamai, E. Rozbicki, M. H. Fischer, J. Voss, P. D. C. King, W. Meevasana, S. Thirupathaiah, E. Rienks, J. Fink *et al.*, New J. Phys. **15**, 063029 (2013).

[20] E. Pavarini and I. I. Mazin, Phys. Rev. B **74**, 035115 (2006).

[21] M. W. Haverkort, I. S. Elfimov, L. H. Tjeng, G. A. Sawatzky, and A. Damascelli, Phys. Rev. Lett. **101**, 026406 (2008).

[22] C. N. Veenstra, Z. H. Zhu, M. Raichle, B. M. Ludbrook, A. Nicolaou, B. Slomski, G. Landolt, S. Kittaka, Y. Maeno, J. H. Dil *et al.*, Phys. Rev. Lett. **112**, 127002 (2014).

[23] G. Zhang, E. Gorelov, E. Sarvestani, and E. Pavarini, Phys. Rev. Lett. **116**, 106402 (2016).

[24] G. Zhang and E. Pavarini, Phys. Rev. B **95**, 075145 (2017).

[25] X. Deng, K. Haule, and G. Kotliar, Phys. Rev. Lett. **116**, 256401 (2016).

[26] M. Schmidt, T. R. Cummins, M. Bürk, D. H. Lu, N. Nücker, S. Schuppler, and F. Lichtenberg, Phys. Rev. B **53**, R14761(R) (1996).

[27] S. Nakatsuji and Y. Maeno, Phys. Rev. Lett. **84**, 2666 (2000).

[28] A. P. Mackenzie, S. R. Julian, A. J. Diver, G. J. McMullan, M. P. Ray, G. G. Lonzarich, Y. Maeno, S. Nishizaki, and T. Fujita, Phys. Rev. Lett. **76**, 3786 (1996).

[29] A. P. Mackenzie, S. Ikeda, Y. Maeno, T. Fujita, S. R. Julian, and G. G. Lonzarich, J. Phys. Soc. Jpn. **67**, 385 (1998).

[30] A. P. Mackenzie, S. R. Julian, G. G. Lonzarich, Y. Maeno, and T. Fujita, Phys. Rev. Lett. **78**, 2271 (1997).

[31] T. Kondo, M. Ochi, M. Nakayama, H. Taniguchi, S. Akebi, K. Kuroda, M. Arita, S. Sakai, H. Namatame, M. Taniguchi *et al.*, Phys. Rev. Lett. **117**, 247001 (2016).

[32] Y. Maeno, S. Kittaka, T. Nomura, S. Yonezawa, and K. Ishida, J. Phys. Soc. Jpn. **81**, 011009 (2012).

[33] A. Damascelli, D. H. Lu, K. M. Shen, N. P. Armitage, F. Ronning, D. L. Feng, C. Kim, Z.-X. Shen, T. Kimura, Y. Tokura *et al.*, Phys. Rev. Lett. **85**, 5194 (2000).

[34] D. H. Lu, M. Schmidt, T. R. Cummins, S. Schuppler, F. Lichtenberg, and J. G. Bednorz, Phys. Rev. Lett. **76**, 4845 (1996).

[35] H. Iwasawa, Y. Yoshida, I. Hase, S. Koikegami, H. Hayashi, J. Jiang, K. Shimada, H. Namatame, M. Taniguchi, and Y. Aiura, Phys. Rev. Lett. **105**, 226406 (2010).

[36] S. Liu, H. Weng, D. Mou, W. Zhang, Q. Wu, J. He, G. Liu, L. Zhao, H. Liu, X. Jia *et al.*, Phys. Rev. B **86**, 165112 (2012).

[37] T. Vogt and D. J. Buttrey, Phys. Rev. B **52**, R9843(R) (1995).

[38] E. J. Rozbicki, J. F. Annett, J.-R. Souquet, and A. P. Mackenzie, J. Phys.: Condens. Matter **23**, 094201 (2011).

[39] M. Behrmann, C. Piefke, and F. Lechermann, Phys. Rev. B **86**, 045130 (2012).

[40] T. Oguchi, Phys. Rev. B **51**, 1385 (1995).

[41] D. J. Singh, Phys. Rev. B **52**, 1358 (1995).

[42] E. Z. Kurmaev, S. Stadler, D. L. Ederer, Y. Harada, S. Shin, M. M. Grush, T. A. Callcott, R. C. C. Perera, D. A. Zatsepin, N. Ovechkina *et al.*, Phys. Rev. B **57**, 1558 (1998).

[43] For a pedagogical introduction, see, e.g., *The LDA+DMFT Approach to Strongly Correlated Materials*, edited by E. Pavarini, E. Koch, D. Vollhardt, and A. Lichtenstein (Verlag des Forschungszentrum Jülich, Reihe, 2011), Vol. 1. For the Coulomb tensor for t_{2g} states, see Chap. 6: http://www.cond-mat.de/events/correl11/manuscripts/pavarini.pdf

[44] P. Blaha *et al.*, WIEN2K, *An Augmented Plane Wave + Local Orbitals Program for Calculating Crystal Properties* (Technische Universität Wien, Austria, 2001); P. Blaha, K. Schwarz, P. Sorantin, and S. Trickey, Comput. Phys. Commun. **59**, 399 (1990).

[45] N. Marzari and D. Vanderbilt, Phys. Rev. B **56**, 12847 (1997).

[46] For the WANNIER90 code, see A. A. Mostofi *et al.*, Comput. Phys. Commun. **178**, 685 (2008). For the interface to WIEN2K, see J. Kunes *et al.*, *ibid.* **181**, 1888 (2010).

[47] H. Shaked, J. D. Jorgensen, O. Chmaissem, S. Ikeda, and Y. Maeno, J. Solid State Chem. **154**, 361 (2000).

[48] E. Gull, A. Millis, A. I. Lichtenstein, A. N. Rubtsov, M. Troyer, and P. Werner, Rev. Mod. Phys. **83**, 349 (2011).

[49] A. N. Rubtsov, V. V. Savkin, and A. I. Lichtenstein, Phys. Rev. B **72**, 035122 (2005).

[50] A. Flesch, E. Gorelov, E. Koch, and E. Pavarini, Phys. Rev. B **87**, 195141 (2013).

[51] M. Jarrell and J. E. Gubernatis, Phys. Rep. **269**, 133 (1996).

[52] A. S. Mishchenko, N. V. Prokof'ev, A. Sakamoto, and B. V. Svistunov, Phys. Rev. B **62**, 6317 (2000); A. S. Mishchenko, in *Correlated Electrons: From Models to Materials*, edited by E. Pavarini, E. Koch, F. Anders, and M. Jarrell, Modeling and Simulation, Vol. 2 (Forschungszentrum Jülich, Jülich, 2012).

[53] T. Yokoya, A. Chainani, T. Takahashi, H. Katayama-Yoshida, M. Kasai, Y. Tokura, N. Shanthi, and D. D. Sarma, Phys. Rev. B **53**, 8151 (1996).

[54] M. Malvestuto, E. Carleschi, R. Fittipaldi, E. Gorelov, E. Pavarini, M. Cuoco, Y. Maeno, F. Parmigiani, and A. Vecchione, Phys. Rev. B **83**, 165121 (2011).

[55] M. Malvestuto, V. Capogrosso, E. Carleschi, L. Galli, E. Gorelov, E. Pavarini, R. Fittipaldi, F. Forte, M. Cuoco, A. Vecchione, and F. Parmigiani, Phys. Rev. B **88**, 195143 (2013).

[56] A. V. Puchkov, Z.-X. Shen, and G. Cao, Phys. Rev. B **58**, 6671 (1998).

[57] H. Guo, Y. Li, D. Urbina, B. Hu, R. Jin, T. Liu, D. Fobes, Z. Mao, E. W. Plummer, and J. Zhang, Phys. Rev. B **81**, 155121 (2010).

[58] O. Gunnarsson, E. Koch, and R. M. Martin, Phys. Rev. B **56**, 1146 (1997); E. Koch, O. Gunnarsson, and R. M. Martin, *ibid.* **60**, 15714 (1999).

[59] Available experiments [60–69] are all in qualitative agreement with each other; they, however, also exhibit some quantitative differences. For example, for Sr_2RuO_4, the dc resistivity is higher in some of the older works; since defects/impurities increase the resistivity, in this work we compare in particular to the recent experimental results of Ref. [60]. For $Sr_3Ru_2O_7$, instead, data from Ref. [68] appear somewhat shifted downwards at high energy with respect to those reported in Ref. [69], but they are in line at low frequency.

[60] D. Stricker, J. Mravlje, C. Berthod, R. Fittipaldi, A. Vecchione, A. Georges, and D. van der Marel, Phys. Rev. Lett. **113**, 087404 (2014).

[61] N. E. Hussey, A. P. Mackenzie, J. R. Cooper, Y. Maeno, S. Nishizaki, and T. Fujita, Phys. Rev. B **57**, 5505 (1998).

[62] Y. Takahashi, S. Chakraverty, M. Kawasaki, H. Y. Hwang, and Y. Tokura, Phys. Rev. B **89**, 165116 (2014).

[63] T. Katsufuji, M. Kasai, and Y. Tokura, Phys. Rev. Lett. **76**, 126 (1996).

[64] J. S. Lee, Y. S. Lee, T. W. Noh, S.-J. Oh, J. Yu, S. Nakatsuji, H. Fukazawa, and Y. Maeno, Phys. Rev. Lett. **89**, 257402 (2002).

[65] A. W. Tyler, A. P. Mackenzie, S. NishiZaki, and Y. Maeno, Phys. Rev. B **58**, R10107(R) (1998).

[66] S. J. Moon, M. W. Kim, K. W. Kim, Y. S. Lee, J.-Y. Kim, J.-H. Park, B. J. Kim, S.-J. Oh, S. Nakatsuji, Y. Maeno *et al.*, Phys. Rev. B **74**, 113104 (2006).

[67] J. A. N. Bruin, H. Sakai, R. S. Perry, and A. P. Mackenzie, Science **339**, 804 (2013).

[68] C. Mirri, L. Baldassarre, S. Lupi, M. Ortolani, R. Fittipaldi, A. Vecchione, and P. Calvani, Phys. Rev. B **78**, 155132 (2008).

[69] J. S. Lee, Y. S. Lee, T. W. Noh, S. Nakatsuji, H. Fukazawa, R. S. Perry, Y. Maeno, Y. Yoshida, S. I. Ikeda, J. Yu, and C. B. Eom, Phys. Rev. B **70**, 085103 (2004).

[70] C. Berthod, J. Mravlje, X. Deng, R. Zitko, D. van der Marel, and A. Georges, Phys. Rev. B **87**, 115109 (2013). As pointed out in this paper, the foot at $2\pi k_B T$ appears as a shoulder in log-log scale.

[71] P. B. Allen, Phys. Rev. B **92**, 054305 (2015).

[72] See, e.g., R. M. Konik and T. M. Rice, Phys. Rev. B **76**, 104501 (2007).

[73] A. Tamai, M. P. Allan, J. F. Mercure, W. Meevasana, R. Dunkel, D. H. Lu, R. S. Perry, A. P. Mackenzie, D. J. Singh, Z. X. Shen, and F. Baumberger, Phys. Rev. Lett. **101**, 026407 (2008).

[74] F. Aryasetiawan, K. Karlsson, O. Jepsen, and U. Schönberger, Phys. Rev. B **74**, 125106 (2006).